Human Brain Mapping

WILEY

RESEARCH ARTICLE OPEN ACCESS

Temporally Defined Brain Network Activation Associated With Slowed Information Processing Speed in Multiple Sclerosis

Olivier Burta[1,2] | Fahimeh Akbarian[1,2] | Chiara Rossi[1,2] | Diego Vidaurre[3,4] | Marie Bie D'hooghe[5] | Miguel D'Haeseleer[5,6] | Guy Nagels[1,2,7] | Jeroen Van Schependom[1,2]

[1]AIMS Lab, Center for Neurosciences, Vrije Universiteit Brussel, Brussels, Belgium | [2]Department of Electronics and Informatics (ETRO), Vrije Universiteit Brussel, Brussels, Belgium | [3]Department of Clinical Medicine, Center of Functionally Integrative Neuroscience, Aarhus University, Aarhus, Denmark | [4]OHBA, Wellcome Centre for Integrative Neuroimaging, Department of Psychiatry, University of Oxford, Oxford, United Kingdom | [5]National Multiple Sclerosis Center, Melsbroek, Belgium | [6]Neurology Department, UZ Brussel, Brussels, Belgium | [7]St Edmund Hall, University of Oxford, Oxford, United Kingdom

Correspondence: Olivier Burta (olivier.burta@vub.be) | Jeroen Van Schependom (jeroen.van.schependom@vub.be)

Received: 19 May 2025 | **Revised:** 30 September 2025 | **Accepted:** 6 February 2026

Keywords: dynamic functional networks | information processing speed | MEG task | multiple sclerosis | symbol digit modalities test | TDE-HMM

ABSTRACT

Information processing speed (IPS) is a core cognitive deficit in people with multiple sclerosis (PwMS). Previous efforts have associated IPS performance to frontal regions, but were constrained by limited temporal resolution. In this work, we employed a data-driven method, the time delay embedded-hidden Markov model (TDE-HMM), to identify task-specific states that are spectrally defined with distinct temporal and spatial profiles. We used magnetoencephalographic (MEG) data recorded while healthy controls and PwMS performed a cognitive task designed to capture IPS, the Symbol Digit Modalities Test (SDMT). The TDE-HMM identified five task-relevant states, supporting a tri-factor contribution to IPS: sensory speed (occipital visual detection and processing), cognitive speed (prefrontal executive and frontoparietal attention shift), and motor speed (sensorimotor). We observed reduced prefrontal activation in PwMS, while peak features across prefrontal, frontoparietal, and occipital networks were associated with task reaction time and clinical SDMT performance. This work can drive future research for MS treatments targeting IPS improvements.

1 | Introduction

Multiple sclerosis (MS) is a leading neuroinflammatory disease in young adults, affecting the central nervous system (CNS) (Dobson and Giovannoni 2019). MS lesions can occur in multiple locations of the CNS, causing a large variety of symptoms ranging from physical to cognitive impairments (Dobson and Giovannoni 2019; Stadelmann et al. 2011). About 50% of people with multiple sclerosis (PwMS) experience cognitive impairment (Julian 2011), affecting domains such as attention, long-term memory, and working memory (Chiaravalloti and DeLuca 2008). However, information processing speed (IPS) stands out as a core cognitive deficit in PwMS (Van Schependom et al. 2015). IPS is the cognitive domain most widely affected by MS (Denney et al. 2008) and is one of the first deficits to emerge (Strober et al. 2009).

The standard cognitive test used to capture IPS deficits is the Symbol Digit Modalities Test (SDMT) (Van Schependom et al. 2014; Benedict et al. 2017). While the original paper-based test remains the standard in clinical practice, computerised adaptations are increasingly being investigated (Middleton et al. 2020). Over the last decade, researchers have turned to using the computerised SDMT as a task paradigm in functional

neuroimaging studies. When studied with functional magnetic resonance imaging (fMRI), PwMS showed greater recruitment of frontal areas during a computerised SDMT, as revealed by network-level effective connectivity (Leavitt et al. 2012). Another fMRI study in people with relapsing–remitting MS (RRMS) found the frontal, superior parietal, occipital, and medial posterior cerebellar areas to activate (Grothe et al. 2020). Compared to healthy controls, Grothe et al. also reported a decreased activation of the cingulate cortex in PwMS during execution of the SDMT (Grothe et al. 2020). However, fMRI is not the optimal functional neuroimaging modality for studying the cognitive processes required during the SDMT due to its temporal unspecificity and being an indirect measure. With a temporal resolution in the range of seconds, fMRI is unable to capture the highly dynamic brain activity involved. As a consequence, the fast-changing patterns of large-scale brain activity underlying SDMT execution, particularly how quickly they unfold over time, remain unclear.

Electrophysiological brain activity can be measured at a much higher temporal resolution. Electroencephalography (EEG) and magnetoencephalography (MEG) capture the electric and magnetic fields generated in the brain as a result of neural activity, respectively. In MS, EEG/MEG has been applied to various cognitive paradigms that, while engaging IPS, rely more heavily on other cognitive domains. For instance, Sarrias-Arrabal et al. used EEG time-frequency analysis of alpha and gamma bands during a visual oddball task, revealing altered early sensory and cognitive processing in MS (Sarrias-Arrabal et al. 2021). During a visuomotor task in MEG, Barratt et al. found delayed post-movement beta rebound and reduced visual gamma oscillations in MS, with the rebound delay correlating with clinical SDMT performance (Barratt et al. 2017). Extending the evidence from oscillatory to evoked-response measures, PwMS displayed a reduced and delayed P3a response during an oddball paradigm, which tracked impairments in IPS (Kiiski et al. 2018). Overall, EEG/MEG studies of IPS-related tasks in MS have primarily focused on individual brain regions or investigated oscillatory activity within specific frequency bands.

Cognition relies on the dynamic interactions of distributed, large-scale brain networks (Bressler and Menon 2010; Liu et al. 2022). Hidden Markov Models (HMMs) offer a powerful framework to capture such transient whole-brain network dynamics, while fully exploiting the high temporal resolution of EEG/MEG (Baker et al. 2014; Quinn et al. 2018). In particular, the time delay embedded-hidden Markov model (TDE-HMM) extends this approach by incorporating temporal autocovariance, enabling the characterisation of fast, transient states of oscillatory brain activity and functional connectivity (Vidaurre, Hunt, et al. 2018). While traditional functional connectivity (FC) analysis methods often fall short in capturing the combined temporal, spectral, and spatial information (Brookes et al. 2014), the TDE-HMM successfully captures this multi-dimensional complexity. This state-of-the-art method has previously been applied in both resting-state (Baker et al. 2014; Vidaurre, Hunt, et al. 2018; Van Schependom et al. 2019) and various task paradigms (Quinn et al. 2018; Rossi et al. 2023; Gohil, Kohl, et al. 2024; Vidaurre, Abeysuriya, et al. 2018). In rest, Vidaurre et al. extracted a frontal and posterior default mode network (DMN) from MEG data (Vidaurre, Hunt, et al. 2018). Using task data enables us to identify the functional brain networks underlying domain-specific cognitive processes. In this context, Rossi et al. unravelled the brain dynamics underlying working memory (WM) in a visual-verbal n-back task (Rossi et al. 2023), showing consistency with existing theoretical models of WM. By further including PwMS in the analysis, they were able to identify pathology-specific and treatment-induced effects captured in the brain states' properties (Rossi et al. 2024).

In this work, we use the TDE-HMM method to study MEG brain activity during a task primarily assessing IPS, the SDMT. Our goal is to provide the first description of the whole-brain networks underlying an IPS task at the millisecond timescale. Further, by including an MS cohort, we aim to identify altered brain dynamics in PwMS, hypothesising that these will be disrupted and likely slowed compared to healthy controls. Finally, we demonstrate how our findings can lend support to existing theories of IPS deficits in MS.

2 | Methods

2.1 | Participants

The dataset consists of 110 subjects, 37 healthy controls (HCs) and 73 people with multiple sclerosis (PwMS). The MS cohort, diagnosed according to the 2010 McDonald criteria (Polman et al. 2011), was recruited at the National MS Center Melsbroek, Belgium. It comprises 63 patients with relapsing–remitting MS (RRMS), 6 with primary progressive MS (PPMS), 3 with secondary progressive MS (SPMS), and 1 with clinically isolated syndrome (CIS). Exclusion criteria included an Expanded Disability Status Scale (EDSS) score greater than 6, or the presence of other neuropsychiatric disorders. Some subjects in the MS cohort are prescribed benzodiazepine (BZD) treatment, known to alter functional brain dynamics (Engelhardt et al. 1992). This dataset contains 18 PwMS with (BZD+) and 55 PwMS without BZD treatment (BZD−). Ethical approval for data collection was provided by the ethical committees of the National MS Center Melsbroek (2015-02-12) and the University Hospital Brussels (Commissie Medische Ethiek UZ Brussel, B.U.N. 143201423263, 2015/11), while retrospective data analysis received ethical approval from the ethical committee of the University Hospital Brussels (B.U.N. 1432025000017, 2025/02).

All participants provided written informed consent and completed a paper version of the SDMT as part of the Brief International Cognitive Assessment in MS (BICAMS) (Benedict et al. 2012) on the MEG session day.

2.2 | MEG and MRI Data

At the start of MEG data collection, a 306-channel Elekta Neuromag Vectorview system in the Laboratoire de Cartographie Fonctionnelle du Cerveau in Erasme Hospital (Belgium) was used (33 subjects). Afterwards, the MEG scanner was upgraded to an Elekta Neuromag Triux scanner (77 subjects). Both scanners sampled the MEG signal at 1000 Hz within a 0.1–330 Hz frequency band. The 306 sensors are arranged in 102 triplets (1 triplet = 1 magnetometer, 1 planar and 1 axial gradiometer). During subject preparation, the Head Position Indicator (HPI)

coil locations, the position of three fiducial points and the head shape were saved using a three-dimensional digitiser (Polhemus). MEG was recorded in a magnetically shielded room (Elekta, MaxShield) to reduce external magnetic interference. Dedicated electro-oculography (EOG) and electrocardiography (ECG) channels were used to measure ocular and cardiac-related activity.

Structural brain information was collected using magnetic resonance imaging (MRI). Scans were acquired using a 3 T Philips MR system at $1\times1\times1\,mm^3$ resolution with T_1-weighted sequence using the following parameters: TR = 4.93 ms, FA 8°, $230\times230\,mm^2$ FOV, 310 sagittal slices, leading to a $0.53\times0.53\times0.53\,mm^3$ resolution. MRI acquisition was performed last to avoid MRI interference with the MEG recording, with a median delay of 5 days between both acquisitions.

2.3 | SDMT Paradigm

During MEG acquisition, subjects performed a computerised SDMT (MEG-SDMT). The key is displayed on a screen, indicating which symbol corresponds to which digit. When the task begins, a first symbol-digit pair is shown, representing a single trial. The subject has at most 6 s to submit a response by pressing one of two buttons (Match/Non-match), indicating whether the shown pair matches one from the key. Subjects were asked to complete the task as fast as possible while minimising mistakes. This task design follows the same outline as proposed by Genova et al. (2009)., but the paradigm used in the present study did not have a fixed interstimulus interval of 3 s. Figure 1 illustrates the task.

Task performance was assessed using two behavioural metrics: reaction time (RT) and response accuracy. The RT is the exact time delay between stimulus presentation and the first recorded button press. The timing of visual stimulus onsets was saved using a photodiode setup located at the bottom of the projector screen. Response accuracy was calculated as the number of correctly responded trials divided by the total number of trials.

Each participant first took a short training to ensure they understood the paradigm. The actual experiment consisted of 128 stimuli, split between 61 Match and 67 Non-match symbol-digit stimuli. Subjects did not receive feedback on their performance during or after the task.

2.4 | MEG Data Processing

MEG data was processed using the OSL toolbox written in Python (OHBA Analysis Group, University of Oxford, UK) (van Es et al. 2025). The pipeline included downsampling to 250 Hz, bandpass and notch filtering, and ICA-based automatic removal of artefactual ocular and cardiac components. Segments of poor-quality data and bad channels were annotated and accounted for during subsequent processing (see Supporting Information, Section 1, Table S1). Source reconstruction was performed with a Linearly Constrained Minimum Variance (LCMV) beamformer on an 8 mm grid, and the resulting data were parcellated into 38 cortical regions. To mitigate magnetic field spread, we applied symmetric orthogonalisation, followed by sign-flipping to resolve dipole ambiguity prior to group-level analysis. For a detailed breakdown of these technical processing steps and the parameters used, see the Supporting Information, Section 3.

2.5 | The Time Delay Embedded—Hidden Markov Model (TDE-HMM)

The Hidden Markov Model (HMM) describes the probabilistic activations of, and transitions between, a set of discrete states that best describe the observed MEG data. Together with their temporal activations, the HMM inference estimates the spatio-spectral properties of the states, which here represent functional brain networks. The Markovian assumption means that, if we knew which state was active at time points $t-1$ and $t+1$, the state activation at time point t would be conditionally independent of all the other time points, given $t-1$ and $t+1$.

Proven to be successful in describing brain dynamic patterns in other task paradigms (Quinn et al. 2018; Rossi et al. 2023), we used the TDE-HMM implementation from the OSL Dynamics Toolbox in Python (Gohil, Huang, et al. 2024). In essence, the TDE-HMM employs a Gaussian distribution on a time-delay embedded (TDE) space. This consists of shifting the original

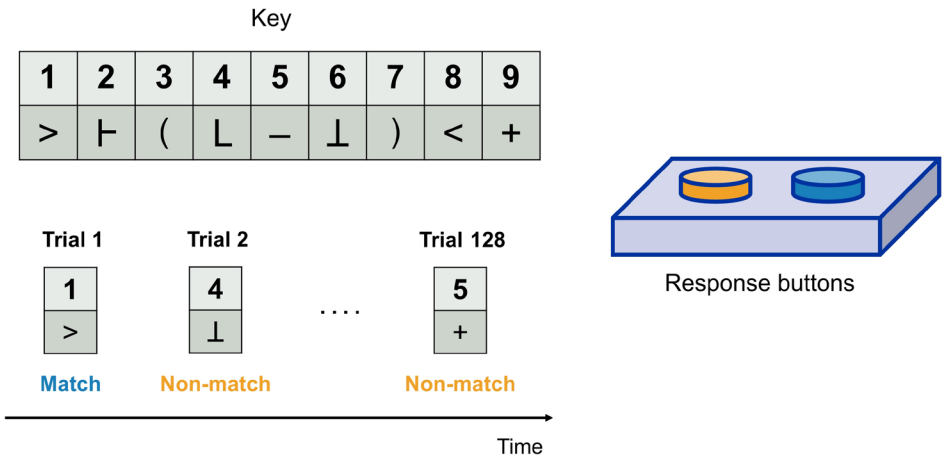

FIGURE 1 | Graphical representation of the workflow during the computerised SDMT. Visual stimuli are presented as symbol-digit pairs. The subject is asked to press the blue button when the presented stimulus matches the key (Match trial), and the orange button in the opposite case (Non-match trial).

data over a set number of lags (here, $N = 15$, spanning lags −7 to +7), allowing the incorporation of past and future time points into each step. Next, the matrix dimensionality is reduced by applying PCA, with the number of principal components at least twice that of the number of parcels (e.g., $38 \times 2 = 76$) (Vidaurre, Hunt, et al. 2018). Afterwards, the data is standardised (i.e., normalised to zero mean and unit variance). With these steps completed, the different model parameters (hidden states time course, transition probability matrix, and observation model) can be learned. These parameters are computed through stochastic variational Bayesian inference (Vidaurre, Abeysuriya, et al. 2018), with updates for small batches of training data to save computations. To ensure that the HMM does not infer parameters from unreliable time series data, the previously labelled bad quality segments were omitted.

The main output consists of the inferred hidden states' time course, providing the probability of each state activating at a given time point in the original MEG data. Subsequently, the time course is one-hot encoded, where each time point is assigned to the state with the highest activation probability, providing the input for subsequent analyses.

When using the TDE-HMM, a pre-specified number of states must be chosen. There is no golden standard for this parameter, it is typically adjusted based on the executed task. In this work, we ran five inferences with 4, 5, 6, 8 and 10 states to assess the influence of this parameter on the provided description.

2.6 | State-Wise Temporal Description

2.6.1 | Averaging and Group-Level Analysis

We conducted an event-related (ER) analysis of the TDE-HMM state time courses to investigate the activation and deactivation dynamics of the inferred states during SDMT execution. Figure 2 illustrates the steps to extract the ER activation of each state. Each trial was epoched between (−500, 3000) ms relative to stimulus onset, given an average RT of around 1.75 s post-stimulus. Epochs that were either incorrectly responded to or contained segments of bad signal quality (Section 2.4) were rejected. The proportion of rejected epochs is reported in the Supporting Information (Section 1, Table S1). Next, for each subject, trials of the same stimulus type (Match or Non-match) were averaged together. To remove baseline differences, the subject-level averages were baseline-corrected by subtracting, for each subject and each state separately, the mean signal in the pre-stimulus (−500, 0) ms period. This procedure yielded a total of 220 subject-level ER time courses (110 subjects × 2 stimulus types), each comprising 6 channels (one per state). Next, we analysed the ER state activations across subjects using a 2nd-level generalised linear model (GLM) to evaluate group-level effects of experimental and subject-specific factors. The 2nd-level GLM design matrix consisted of 6 regressors: a constant regressor (mean activity), four categorical regressors (stimulus type, disease presence, benzodiazepine use, and gender), and one regressor modelling the interaction between stimulus type and disease. The corresponding regression equation and design matrix are provided in the Supporting Information (Section 6, Equation 1 and Figure S3, respectively).

2.6.2 | Contrast Definitions: Task- and Group-Related Effects

Building on the 2nd-level GLM setup, we first identified which states' activation is modulated during the task by evaluating the Mean Effect contrast, reflecting overall task-related activation across subjects (see Figure 2c). Statistical significance was assessed by testing at each time point whether the contrast of parameter estimates (COPEs) significantly differed from zero, using a maximum t-statistic permutation test ($N = 1000$). The maximal t-statistic controls the familywise error rate (Nichols

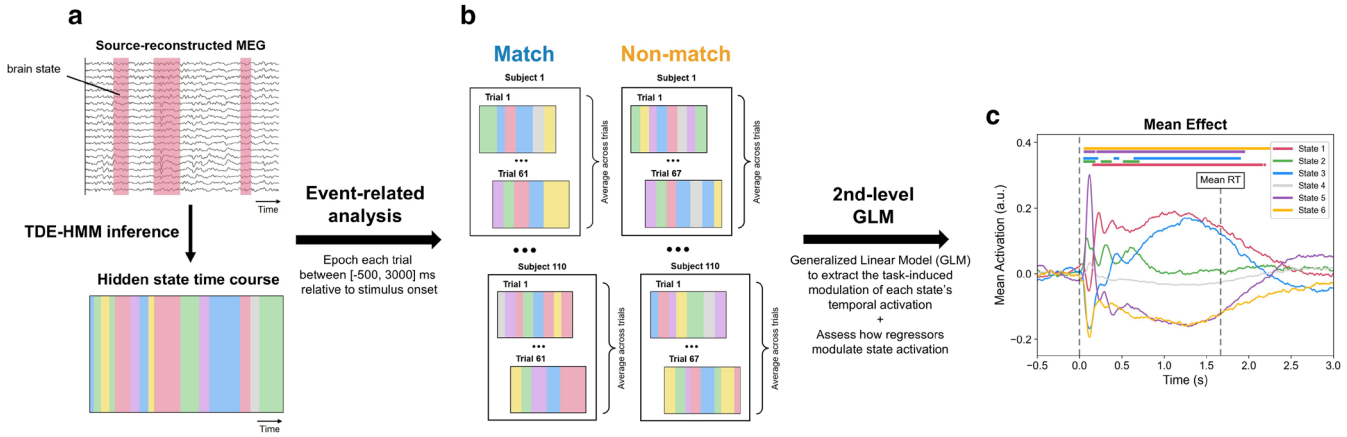

FIGURE 2 | Evoked-response analysis of the six TDE-HMM states. (a) Hidden state time course inferred from MEG. Each time point is assigned to the most likely state to be active. (b) Computing subject-level event-related (ER) state activation profiles. We epoched every trial from 500 ms before to 3000 ms after stimulus onset. Epochs with incorrect responses or segments of bad signal quality were rejected. Trials of the same subject and stimulus type (Match or Non-match) were averaged, and the resulting subject-level averages were baseline-corrected using the pre-stimulus (−500, 0) ms period. (c) Five states were identified as task-related. ER state activations were analysed across subjects using a second-level GLM. The plot displays the Mean Effect contrast, reflecting the overall task-related modulation. Task-related states are those containing time points where the activation time course significantly differs from zero, indicated by the coloured horizontal lines at the top. Significance was determined using a maximum t-statistic permutation test ($N = 1000$), correcting for multiple comparisons across states and time points, with $\alpha = 0.01$.

and Hayasaka 2003), thereby correcting for multiple comparisons across both time points and states.

In our design, the 2nd-level GLM included 9 contrasts (see Supporting Information Section 6, Figure S3). Beyond the Mean Effect contrast, we defined four contrasts (C2–C5 in Figure S3) to examine if the aforementioned group-level and experimental factors significantly modulate state activations. Additionally, we constructed four contrasts (C6–C9 in Figure S3) to test the interaction between stimulus type and disease, allowing us to assess whether group differences in brain state recruitment between HCs and PwMS depend on stimulus type. All contrasts were evaluated using the same maximal *t*-statistic permutation procedure described above, with a significance threshold of 5%.

2.6.3 | Peak Analysis and Relationships With Behavioural Data

For states showing a significant disease effect contrast, we first identified consecutive significant time points. We then defined analysis windows around these ranges, wide enough to capture inter-subject variability in peak latencies, and used them for a peak analysis. Within each time window, we extracted from every subject-level ER time course the maximum (or minimum) peak amplitude and its latency. Group differences between the peak features of HCs and PwMS were assessed using a permutation *t*-test ($N = 1000$), with False Discovery Rate (FDR) correction applied across 20 comparisons (5 peaks × 2 peak features × 2 paradigm conditions). Furthermore, we investigated correlations (Pearson's correlation) between these peak features and behavioural data across all subjects. The behavioural measures were separated into MEG-SDMT (mean reaction time and accuracy from the computerised SDMT performed during MEG) and clinical SDMT (*z*-score from the clinical assessment). Mean RTs and accuracies for the MEG-SDMT were computed separately for Match and Non-match trials. Correlations were corrected for multiple comparisons (via FDR), with a total of 60 correlations (5 peaks × 2 peak features × 2 paradigm conditions × 3 behavioural measures).

2.7 | Spectral and Spatial Characteristics

The spectral properties of the states are extracted using a non-parametric multitaper spectral estimation applied to every subject and state separately (Vidaurre et al. 2016). This method takes the original parcelled MEG data multiplied by the hidden state time course as input, and produces power spectral densities (PSD) as output. These PSDs were originally determined for a wideband frequency range of (1–45) Hz. Subsequently, we estimated the state-specific spatial description by integrating the wideband PSDs over four frequency bands extracted using non-negative matrix factorisation (NNMF) (Quinn et al. 2018). These data-driven frequency bands are referred to as spectral components. To decide which spectral component best describes the spectral properties of a certain state, first, the mean PSD and mean coherence (averaged across all subjects and brain parcels) were plotted as a function of frequency, for that state. Next, similarity was sought in the frequency ranges between each data-driven spectral component and the frequency range of the strongest peak in both mean PSD and mean coherence plots. To plot the PSDs as spatial maps, each state-specific PSD was weighted with the most relevant spectral component for that state. We then took the weighted power, averaged it across all subjects, and report the spatial profiles as a *z*-score PSD distribution across brain parcels.

To quantify spectral synchronisation between brain regions, the PSDs were used to compute the coherence at each frequency bin, as explained by Vidaurre, Hunt, et al. (2018). The obtained coherence networks are state-specific, scaled by the most relevant spectral component for each state. For visualisation, only the connections remaining after Gaussian mixture model (GMM) thresholding are shown on both a circular plot and a brain mask.

3 | Results

3.1 | Behavioural Data

The demographic and clinical characteristics of different subgroups in this study are shown in Table 1. The HC and PwMS groups are matched on gender (χ^2 test, p-value = 0.18) and age (Mann–Whitney *U*-test, p-value = 0.84). The mean education level (Mann–Whitney *U*-test, p-value = 0.005) and SDMT score (Mann–Whitney *U*-test, p-value = 0.007) are significantly higher for HCs compared to PwMS in this dataset. The BZD+ and BZD− groups within the MS cohort significantly differ in terms of gender (Fisher exact test, p- value = 0.004) and EDSS score (Mann–Whitney *U*-test, p-value = 0.040).

In terms of task performance, PwMS performed significantly worse than HCs, with mean response accuracies of 97.1% ± 2.3% for PwMS and 98.1% ± 1.7% for HCs (Mann–Whitney *U*-test, $p = 0.015$; see Supporting Information Section 2, Figure S1). Subjects overall did not differ in accuracy between Match and Non-match trials, although PwMS made significantly more errors on Non-match trials compared to Match trials (see Supporting Information Section 2, Table S2). Reaction times (RTs) were significantly longer for Non-match (1.82 ± 0.38 s) than Match trials (1.67 ± 0.32 s) across all participants, including within each group. Furthermore, PwMS responded significantly slower than HCs regardless of stimulus type (see Supporting Information Section 2, Table S3).

3.2 | Model Inference

The TDE-HMM was run five times to infer 4, 5, 6, 8 and 10 states from the MEG data separately, allowing to assess the model's robustness (Alonso and Vidaurre 2023). The choice of hyperparameters for both the data preparation (time embedding, PCA) and the inference process can be found in the Supporting Information (Section 4, Table S4). We observed that the 8 and 10 states inference provided some states with overlapping temporal and spatial characteristics. While

TABLE 1 | Demographic and clinical characteristics of the SDMT dataset.

	HCs	PwMS	*p*	BZD+	BZD−	*p*
N	37	73	N/A	18	55	N/A
% female	59.46	73.97	0.18	100	65.45	**0.004***
Age (years)	47 ± 12	48 ± 10	0.84	48 ± 8	48 ± 10	0.94
Education (years)	15 ± 2	14 ± 3	**0.005***	13 ± 3	14 ± 3	0.26
SDMT score	54.5 ± 9.4	48.6 ± 10.7	**0.007***	47.1 ± 7.5	49.1 ± 11.6	0.49
Disease dur. (years)	N/A	16.6 ± 9.8	N/A	13.4 ± 6.8	17.7 ± 10.4	0.11
EDSS	N/A	3.2 ± 1.5	N/A	3.8 ± 1.1	3.1 ± 1.6	**0.040***

Note: Statistical comparisons were conducted between healthy controls (HCs) and people with multiple sclerosis (PwMS), with an additional group comparison between BZD+ (PwMS with BZD treatment) and BZD− (PwMS without BZD treatment). Age, education, SDMT score (on-paper Symbol Digit Modalities Test), disease duration, and EDSS (Expanded Disability Status Scale) are reported as mean ± std. Differences in continuous outcomes across groups were compared using the Mann–Whitney *U*-test.
Abbreviation: N/A, not applicable.
*$p < 0.05$.

further increasing the number of states may lead to some highly similar states, reducing the number of states may offer a too coarse solution, with distinct functional networks collapsing into the same state. In our data, we found that the 6-state solution strikes a good balance, and the results from this solution are shown and discussed.

The stochastic nature of the variational Bayesian inference process (Brookes et al. 2014) requires us to assess the stability and replicability of our results. Therefore, we trained the 6-state model four separate times. We determined the model inference to be stable, as states with similar spatiotemporal characteristics were consistently retrieved. Additionally, several summary statistics, describing the general dynamics of the states' activation over the entire inference, are reported in the Supporting Information (Section 5, Figure S2 and Table S5).

3.3 | Task-Related Brain States

Figure 2c shows the average task-evoked state activation profiles during the computerised SDMT. The task-relevant states are those that are significantly activated or deactivated throughout the considered epoch window: states 1, 2, 3, 5, and 6 are task-related. State 4 reflects lateral occipital baseline activity with properties (summary metrics, spatial profile) consistent with TDE-HMM literature (Quinn et al. 2018), and its description is reported in the Supporting Information (Section 10, Figure S12).

In addition to the Mean Effect contrast, we tested four contrasts probing main effects of stimulus type, disease, benzodiazepine use, and gender on the states' ER activation profiles. Results for these contrasts are reported in the Supporting Information (Section 6, Figure S4). We also evaluated four contrasts testing the interaction between stimulus type and disease, to assess whether group differences in brain state recruitment depend on task demands. Results of these interaction contrasts are likewise provided in the Supporting Information (Section 6, Figure S5).

3.4 | Spectral Contents

Four spectral components were extracted from the data, with their profiles reported in the Supporting Information (Section 9, Figure S8). These findings are consistent with those reported in previous TDE-HMM studies (Vidaurre, Hunt, et al. 2018; Rossi et al. 2023). The three relevant spectral components, primarily representing the low-frequencies (1–8 Hz), alpha band (8–13 Hz), and beta band (13–30 Hz), were used to extract the weighted state-specific spatial maps and spectral coherence networks.

The state-specific mean PSD (Figure 3a) and mean coherence (Figure 3b) across all subjects were used to determine which spectral component best describes the properties of a particular state.

3.5 | Description of Brain States

3.5.1 | State 1

State 1 shows a task-related response significantly activated between 250 and 1250 ms post-stimulus (Figure 2c). After that, the mean activation probability gradually decreases until 2250 ms post-stimulus. The activity of state 1 is mostly contained within spectral component 1, as can be seen from the low-frequency peak in both PSD (Figure 3a) and coherence (Figure 3b). From the *z*-scored PSD map, mainly frontal regions show the highest power. The coherence networks reveal the involvement of prefrontal (e.g., superior, ventrolateral, orbitofrontal), medial sensorimotor, posterior cingulate cortex (PCC), and anterior temporal regions.

3.5.2 | State 2

State 2 significantly activates at 300 ms post-stimulus, with a second significant peak around 550 ms post-stimulus (Figure 2c). Distinct alpha peaks in both mean PSD (Figure 3a) and coherence plots (Figure 3b) lead to this state being associated with

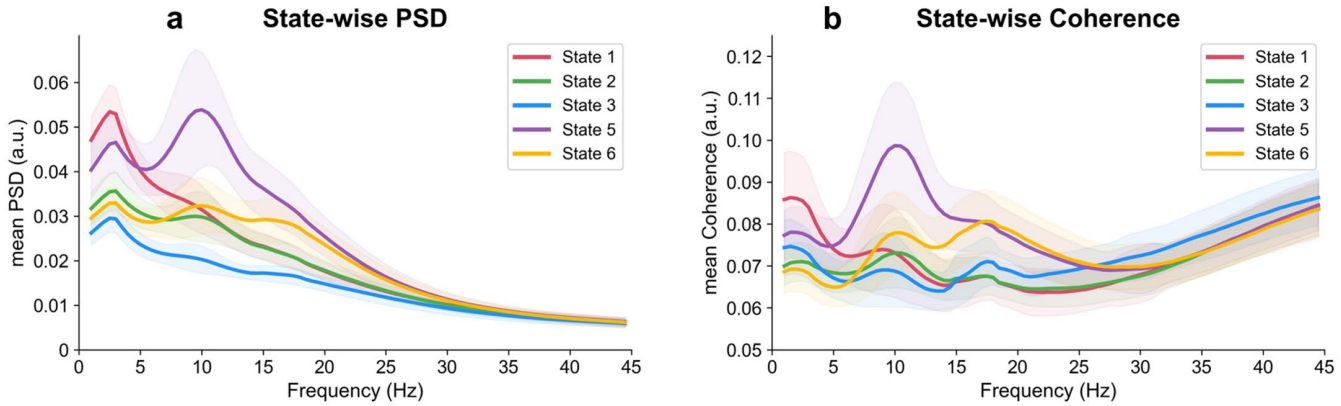

FIGURE 3 | State-wise (a) mean power spectral density (PSD) and (b) mean coherence for only the task-relevant states. PSD and coherence are averaged across subjects and across all regions (PSD) or pairs of regions (coherence). Shaded areas at each frequency bin correspond to the standard deviation across subjects.

spectral component 2. The spatial PSD map highlights the occipital lobe. This is further supported by the coherence networks showing high synchronisation between several regions in the occipital brain area. More specifically, this concerns the inferior occipital, middle occipital, occipital pole, and cuneus regions, with multiple connections spanning across the two hemispheres. For TDE-HMM runs with a lower number of hidden states ($k=4$, $k=5$), state 2 and state 5 collapse into a single occipital state.

3.5.3 | State 3

State 3 is characterised by a significant increase in activation at 450 ms post-stimulus, followed by sustained activation between 750 and 1500 ms (Figure 2c). We also observed a significant deactivation around 100 ms post-stimulus, which may reflect the mutual exclusivity assumption (i.e., when other states such as state 2 and 5 in the presented results are strongly activated, the remaining states show relative deactivation with respect to baseline). On the spatio-spectral level, state 3 represents a frontoparietal network characterised by broadband coherence. While the mean PSD (Figure 3a) appears rather flat across all frequencies, the mean coherence (Figure 3b) displays small peaks for each spectral component's frequency range. With the beta range peak standing out the most, we determined state 3's spectral content to be mainly focused on beta activity. State 3 activates in the frontal (ventrolateral and dorsal prefrontal cortex) and parietal (supramarginal gyrus) lobes. Coherence networks display broad connectivity patterns, with consistently retrieved parieto-occipital coherence in all three spectral components (Figure S11).

3.5.4 | State 5

State 5 is characterised by the strongest significant activation between 50 and 100 ms post-stimulus across all states (Figure 2c). This is followed by significant deactivation between 300 and 1750 ms post-stimulus. Similarly to state 2, state 5 is characterised by alpha activity (spectral component 2) in the occipital lobe. Its coherence network is similar to that of state 2, although the connectivity strength in state 5 is overall stronger.

3.5.5 | State 6

State 6 significantly deactivates between 100 and 1300 ms post-stimulus, after which reactivation builds up (Figure 2c). This reactivation occurs about 450 ms before the mean RT to the stimuli (1750 ms post-stimulus). Based on a peak in the PSD (Figure 3a) and the strongest coherence peak (Figure 3b), both in the beta frequency range, the main spectral content of state 6 is summarised by spectral component 3. The spatial PSD map of state 6 displays activity in the supramarginal sensorimotor cortex, present in both hemispheres. On top of the regions identified through the spatial map, the coherence networks display strong connections between the left and right superior prefrontal, and the left and right angular gyri. Notably, the lateral and medial sensorimotor cortices show inter-hemisphere connections.

3.6 | Group-Level Differences and Correlations

3.6.1 | Temporal State Activation Differences

Figures 4 and 5 show time points where activation profiles significantly differed between PwMS and HCs (max t-stat permutation, $N=1000$, $p<0.05$). State 1, representing a prefrontal network, showed a significantly increased activation in HCs around 200–250 ms post-stimulus (Figure 4a). The frontoparietal network (state 3) exhibited significantly stronger activation in PwMS across most of the epoch window (Figure 4e). Lastly, the occipital state 5 was significantly less activated in PwMS between 50–100 ms, 450–650 ms, and 1300–2200 ms post-stimulus (Figure 5a). Based on these findings, we defined peak windows for subsequent analyses: state 1 (early activation, 150–350 ms), state 3 (early activation, 350–600 ms; late activation, 850–1750 ms), and state 5 (early activation, 50–200 ms; late deactivation, 1000–2000 ms).

3.6.2 | Peak Analysis and Correlations With Behavioural Data

Figure 6 shows the distributions of peak features (amplitude and latency) extracted in five peak windows. This analysis revealed

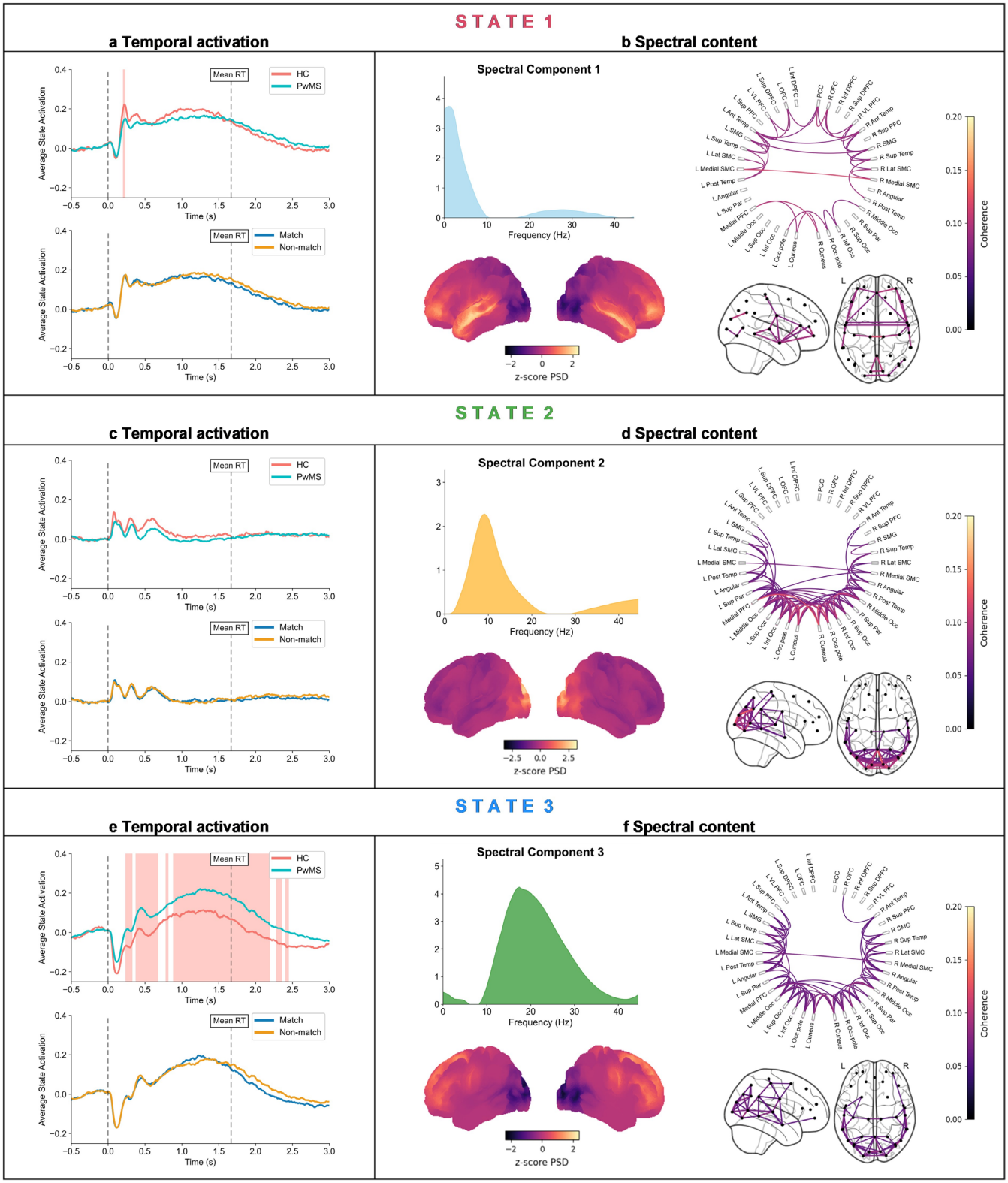

FIGURE 4 | Description of state 1, 2, and 3. We report the (a, c, e) temporal activation pattern and (b, d, f) spectral content of each state. The temporal activation profile plots for (a) state 1, (c) state 2, and (e) state 3 each display two comparisons: Disease group (HCs vs. PwMS) and paradigm condition (Match vs. Non-match), with solid lines representing the group-averaged epochs. Dotted vertical lines indicate the stimulus onset and mean reaction time, while pink shaded areas highlight time points where GLM contrasts reveal significant differences across groups or task conditions (max t-stat permutation, $N = 1000$, $p < 0.05$). Next, the spectral content boxes of (b) state 1, (d) state 2, and (f) state 3 contain: the spectral component best associated with the state, the group-level average PSD map, and the coherence network. The z-score PSD (standardised across parcels) was computed within the relevant spectral component's weighted frequency range. Lastly, the coherence networks are shown as circular plots and through brain masks. Only connections surviving thresholding via GMM are displayed.

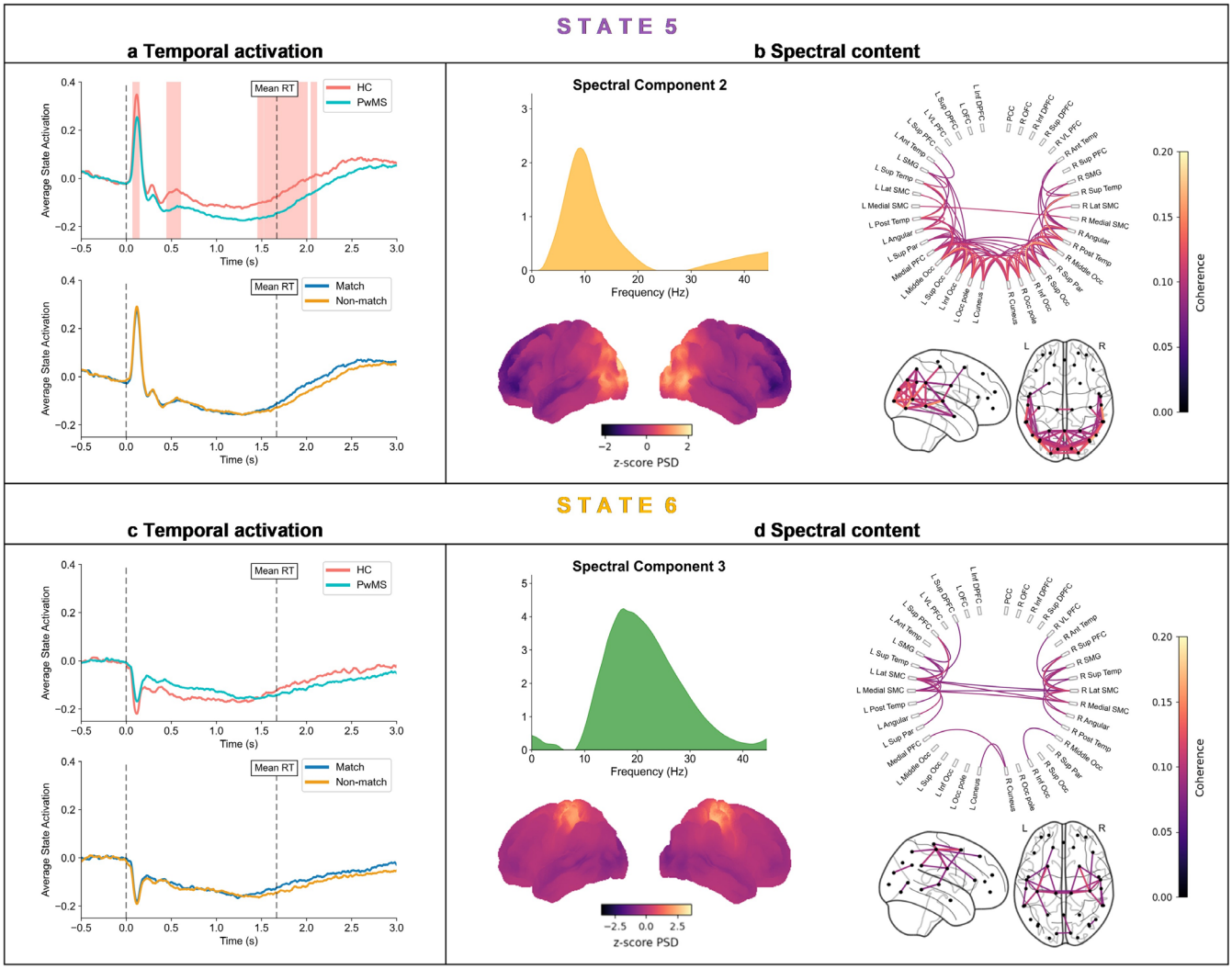

FIGURE 5 | Description of state 5 and 6. We report the (a, c) temporal activation pattern and (b, d) spectral content of each state. The temporal activation profile plots for (a) state 5 and (c) state 6 each display two comparisons: Disease group (HCs vs. PwMS) and paradigm condition (Match vs. Non-match), with solid lines representing the group-averaged epochs. Dotted vertical lines indicate the stimulus onset and mean reaction time, while pink shaded areas highlight time points where GLM contrasts reveal significant differences across groups or task conditions (max t-stat permutation, $N = 1000$, $p < 0.05$). Next, the spectral content boxes of (b) state 5 and (d) state 6 contain: The spectral component best associated with the state, the group-level average PSD map, and the coherence network. The z-score PSD (standardised across parcels) was computed within the relevant spectral component's weighted frequency range. Lastly, the coherence networks are shown as circular plots and through brain masks. Only connections surviving thresholding via GMM are displayed.

the maximum amplitude of state 1's early activation peak in Match trials to be significantly reduced in PwMS. When relating this peak feature to behavioural measures from all subjects (MEG-SDMT reaction time (RT) and accuracy, and clinical SDMT performance), we found a significant negative correlation with RT, consistent across both stimulus types (Figure 7a). This correlation was stronger in Match ($r = -0.396$, $p = 6e\text{-}4$) than in Non-Match trials ($r = -0.299$, $p = 0.018$), as indicated by Steiger's test for dependent correlations (Steiger 1980) ($z = -2.34$, $p = 0.019$). In addition, this same peak feature was significantly positively correlated with clinical SDMT z-scores, but only in Non-match trials. Thus, higher amplitudes of early prefrontal activation were linked with faster responses and better cognitive performance on the SDMT.

In the frontoparietal state 3, peak features of both early and late activations did not reveal significant differences between HCs and PwMS. Further, HCs show a trend toward shorter latencies of the late activation peak in Match compared to Non-match trials (Figure 6). Importantly, the maximum latency of the late activation peak was significantly correlated with MEG-SDMT RTs in Match trials, but not in Non-match trials (Figure 7c).

For the occipital alpha state 5, characterised by an early activation (50–100 ms post-stimulus) followed by sustained deactivation (Figure 2c), significant associations with behavioural measures emerged only during the late deactivation phase (Figure 8b). Specifically, the minimum latency of the late peak significantly positively correlated with RT in both Match ($r = 0.406$, $p = 4e\text{-}4$) and Non-Match trials ($r = 0.310$, $p = 0.015$), with no significant difference in correlation strength between conditions (Steiger's test, $z = 1.38$, $p = 0.17$). In Non-match trials only, this same feature also showed a significant negative correlation with clinical SDMT scores, indicating that later

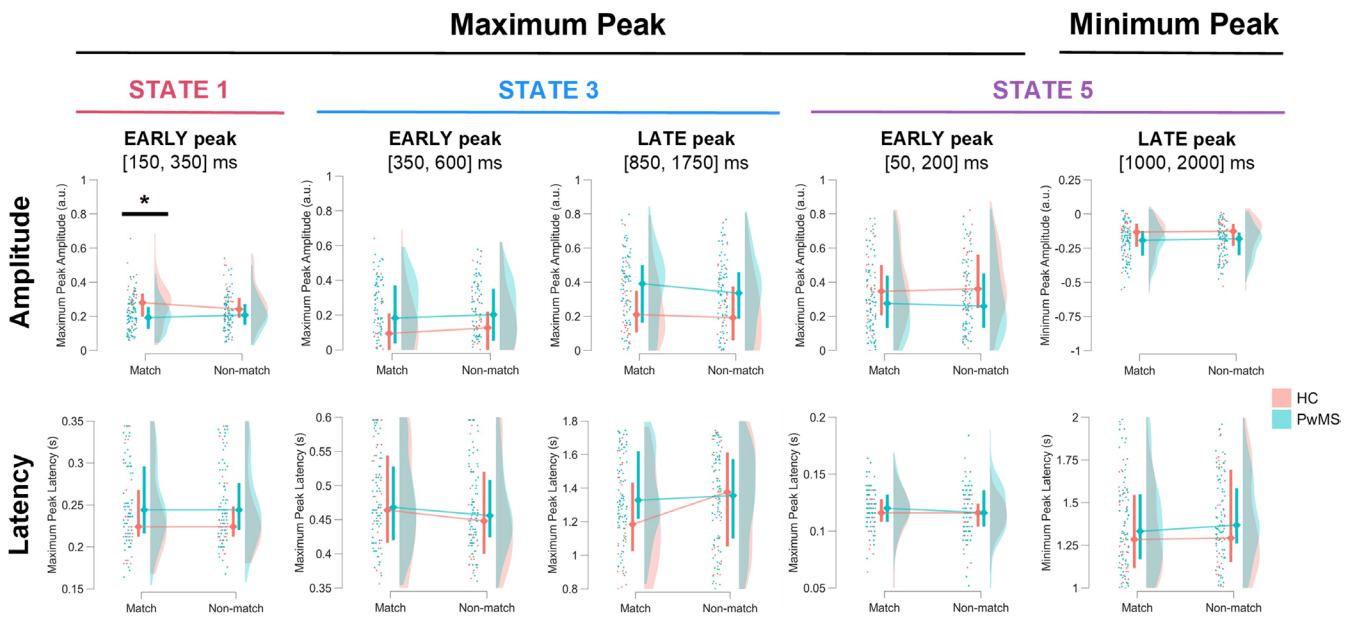

FIGURE 6 | PwMS show reduced early activation maximum peak amplitude in state 1 during Match trials. Distributions of event-related (ER) features—amplitude (top row) and corresponding latency (bottom row) – extracted at the maximum or minimum peaks of states 1, 3, and 5. Each violin plot represents the distribution of subject-level peak features for one group (HCs or PwMS) and a single paradigm condition (Match or Non-match), with individual subject data points overlaid as dots and a 25%–75% interquartile range boxplot shown. Only correctly responded trials were included when computing subject-level ER state activations. Black bold horizontal lines indicate significant between-group differences (permutation *t*-test, FDR corrected across 20 comparisons, $p < 0.05$).

minimum peaks were associated with poorer IPS performance. As the late activation peak in state 3 (850–1750 ms) and the late deactivation peak in state 5 (1000–2000 ms) both occur in a later phase, show substantial temporal overlap, and display the same behavioural trend of increased latency being associated with longer RTs, we examined whether their latencies were related (during Match trials). The latency measures were significantly correlated ($r = 0.461$, $p = 4e\text{-}7$; see Figure S17).

4 | Discussion

In this work, we used the TDE-HMM to extract data-driven brain states with distinct spectral profiles involved during SDMT execution. By leveraging the fast temporal resolution of EEG/MEG, this approach provides a network-level description of the transient whole-brain dynamics supporting IPS, a core cognitive deficit in PwMS. So far, fMRI studies have consistently reported strong activation of the frontal, parietal, and occipital lobes in healthy individuals (Forn et al. 2009; Silva et al. 2018). In clinical populations with impaired IPS, such as PwMS, increased frontal recruitment and enhanced connectivity are particularly evident during early disease stages (Leavitt et al. 2012). Another study reported reduced cingulate cortex activation, interpreted as diminished attentional drive, in PwMS compared to healthy controls (Grothe et al. 2020). However, these studies could not capture the fast temporal dynamics underlying SDMT execution. In the following, we discuss the extracted TDE-HMM states in their order of activation throughout the task.

Visual stimuli presented during the SDMT are first captured in the occipital cortex. State 5's activation at a latency of 100 ms resembles the P100 visual-evoked potentials (VEPs) reported in literature (Caffarra et al. 2024; Schlaeger et al. 2012). This occipital state is mainly characterised by alpha activity, previously associated with the initial detection of visual stimuli (Pokryszko-Dragan et al. 2015; Foxe and Snyder 2011). The VEP literature repeatedly reports prolonged latencies and reduced amplitudes in the P100 responses of PwMS (Ichihara-Takeda et al. 2015; Fuster 2001). Although we found a reduced event-related occipital state activation in PwMS compared to HCs (Figure 5a), our peak analysis did not reveal significant differences in early peak amplitude or latency between these cohorts.

The late deactivation in this occipital state may reflect mechanisms of sensory suppression during periods of heightened cognitive demand, as has been described in studies of occipital alpha activity (Foxe and Snyder 2011; Ichihara-Takeda et al. 2015). Behaviourally, this late peak latency was associated with longer MEG-SDMT reaction times across both stimulus types, and with poorer clinical SDMT performance, specifically in Non-match trials (Figure 8b). At the same time, methodological factors may contribute to this effect: given the mutual exclusivity imposed by the HMM framework, the use of baseline correction at the subject level, and the strong correlation between the latencies of the late peaks in state 3 and state 5 (Figure S17), part of the observed association could arise from interdependencies between state definitions rather than reflecting fully independent processes.

Following the initial stimulus detection, a prefrontal network activates at 250 ms post-stimulus and persists until 1500 ms post-stimulus. State 1 arises predominantly in the prefrontal cortex, consistent with fMRI findings (Grothe et al. 2020; Forn et al. 2009; Silva et al. 2018). The prefrontal cortex plays a crucial role in numerous cognitive processes, including

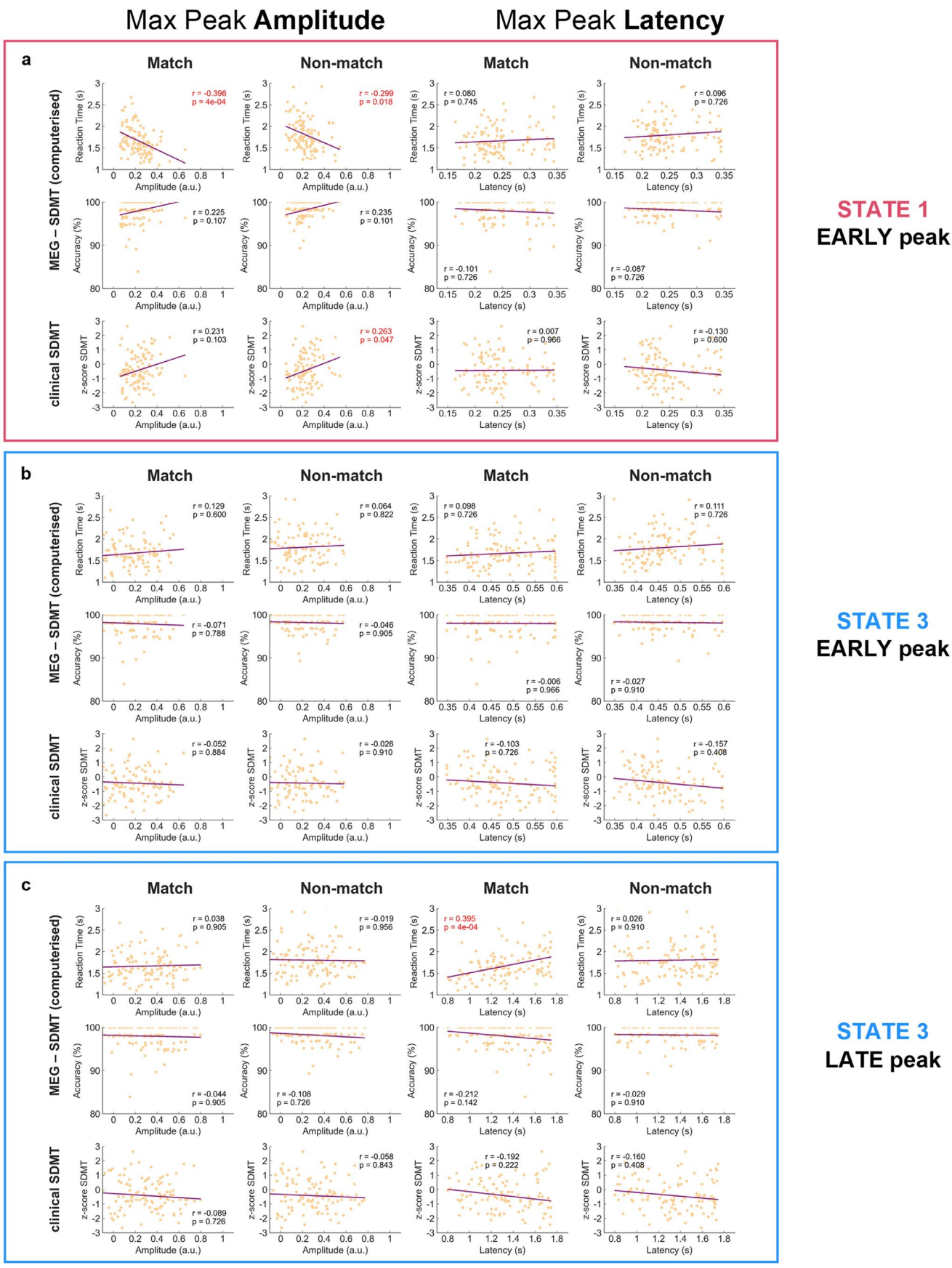

FIGURE 7 | Legend on next page.

FIGURE 7 | Correlations between state activation peak features and behavioural data. Each panel shows correlations for both amplitude and latency of the maximum peaks: (a) early peak of state 1, (b) early peak of state 3, (c) and late peak of state 3. Correlations were computed separately for Match and Non-match trials. Behavioural measures are separated into MEG-SDMT (mean reaction time and accuracy from the computerised SDMT performed during MEG) and clinical SDMT (*z*-score from the clinical assessment). Relationships are displayed as scatter plots and regression lines, whose correlation coefficient (*r*) is computed using Pearson's correlation. *p*-values (*p*) were corrected for multiple comparisons using FDR ($N = 60$).

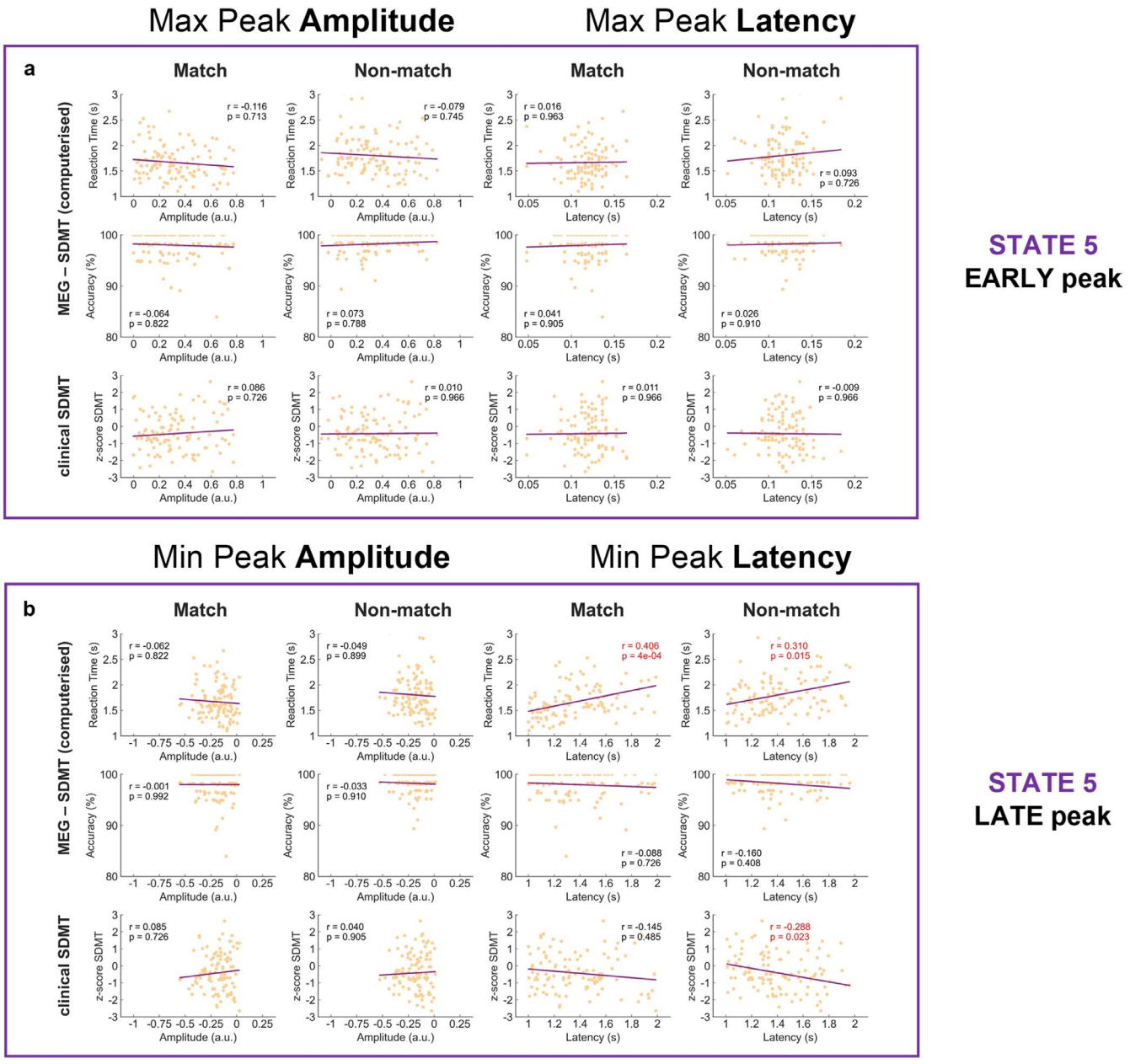

FIGURE 8 | Correlations between state activation peak features and behavioural data. Each panel shows correlations for both amplitude and latency of the (a) maximum early peak of state 5, and (b) minimum late peak of state 5. Correlations were computed separately for Match and Non-match trials. Behavioural measures are separated into MEG-SDMT (mean reaction time and accuracy from the computerised SDMT performed during MEG) and clinical SDMT (*z*-score from the clinical assessment). Relationships are displayed as scatter plots and regression lines, whose correlation coefficient (*r*) is computed using Pearson's correlation. *p*-values (*p*) were corrected for multiple comparisons using FDR ($N = 60$).

stimulus encoding, information integration, and goal-directed behaviour, as well as in emotional regulation (Fuster 2001; Dixon et al. 2017). Most of this state's spectral content is described within the low-frequencies, specifically the theta range. Given that prefrontal theta activity has been widely associated with memory encoding and higher-order cognitive processing (Nuñez and Buño 2021; Tamura et al. 2017), this state could play a role in stimulus encoding during the

SDMT. Another cognitive process often associated with executive frontal regions is that of decision-making (Andersen and Cui 2009; Broche-Pérez et al. 2016). Considering that state 1 remains significantly activated until 300 ms before the mean RT, this could capture the response button selection near the end of an SDMT trial.

We found that PwMS show significantly reduced activation of this prefrontal network compared to HCs, only at early state activation (250 ms post-stimulus). Decreased prefrontal activation was previously reported using fMRI (Genova et al. 2009), and more recently in a follow-up study by Rossi et al. using the same TDE-HMM approach during a working memory task (Rossi et al. 2024). Impaired functional activation of state 1 could be a result of structural brain damage (Meijer et al. 2018). As such, Grothe et al. have shown an association between IPS performance and structural white matter damage in frontoparietal regions in PwMS (Grothe et al. 2022). Our work also revealed significant correlations between maximum peak features of prefrontal state activation and MEG-SDMT reaction times, as well as clinical SDMT performance. This further suggests that the integrity of the executive control unit in the prefrontal cortex contributes to slowed IPS in PwMS (Kouvatsou et al. 2022).

In the next phase of the SDMT, the presented stimulus is compared against the key. The extracted state 3, representing a frontoparietal network, may play a crucial role in this process. Previous studies have associated parietal activations with spatial attention shifts during visual tasks (Corbetta et al. 1995; Corbetta 1998). Other research has linked functional connectivity between occipital and parietal regions with visual information processing (Pisarchik et al. 2019; Küchenhoff et al. 2021). Given that our frontoparietal state is characterised by a parieto-occipital coherence network, this points to its involvement in visual stimulus processing during the SDMT.

This is reinforced by looking at the successive significant activations of state 2 (occipital) and state 3 (frontoparietal) depicted in Figure 2c. Specifically, the occipital state first activates at 300 ms post-stimulus, followed by the frontoparietal state at 450 ms, and again occipital activation at 550 ms. One could hypothesise that the frontoparietal activation around 450 ms supports spatial shift guiding oculomotor control between the stimulus and the code above. Yet, oculographic data was not available to test this hypothesis. In addition, our results show that both states exhibit parieto-occipital coherence in the alpha band (Figures S10 and S11). This aligns with findings by Zhigalov et al. who suggest that alpha oscillations facilitate visual information gating between parieto-occipital regions (Zhigalov and Jensen 2020), supporting our hypothesis.

Alongside alpha-coherence, this frontoparietal state is further marked by beta-coherence. Antzoulatos et al. propose that beta-band synchrony within frontoparietal networks is crucial for maintaining task-relevant representations, as demonstrated during a visual categorisation task (Antzoulatos and Miller 2016). In the SDMT paradigm, frontoparietal activation between 750 and 1500 ms post-stimulus may reflect the mental processes involved in categorising the presented stimulus as a match or non-match relative to the key. This categorisation could then inform decision-making by the prefrontal network, as indicated by the simultaneous event-related activation patterns in both frontoparietal and prefrontal states. Interestingly, the main analysis (6-state model) revealed a frontoparietal network containing both alpha and beta coherence, which remained within a single state even when expanding the model to infer more states ($k = 10$). This may suggest one of two potential explanations: that these processes are inherently interrelated, or that this reflects a methodological limitation of our approach.

Compared to HCs, PwMS exhibit a significantly increased temporal activation of the frontoparietal state, maintained across the full epoch window (Figure 4e). A review by Rocca et al. highlights increased frontoparietal fMRI activity in PwMS who maintain intact performance during cognitive tasks (Rocca et al. 2022). This is consistent with the theory of compensatory network activations in neurological diseases (Kanishka and Jha 2023), where increased frontoparietal activity may reflect the brain's attempt to sustain cognitive performance despite MS-induced dysfunction. When examining maximum peak features within this state, however, no significant group differences were observed, indicating that overall temporal activation increases picked up by the 2nd-level GLM do not necessarily translate into altered peak amplitudes or latencies. Importantly, the maximum latency of the late activation peak in this frontoparietal state was significantly correlated with task reaction times in Match trials (Figure 7c), such that longer latencies were associated with slower responses. This result suggests that, beyond overall increases in frontoparietal activation, subtle temporal dynamics of the late peak are linked to reaction time, indicating that temporal variability in frontoparietal activation is behaviourally relevant.

The final step in the task paradigm consists of reporting whether the presented stimulus matches the key by pressing one of two buttons. The spatio-spectral layout of state 6 corresponds to a typical sensorimotor network, characterised by beta activity in the left and right somatosensory cortices (Jensen et al. 2005). Previous TDE-HMM studies reported similar states in MEG task paradigms requiring a motor response (Quinn et al. 2018; Rossi et al. 2023).

Overall, we identified five brain states relevant to computerised SDMT execution, each having distinct temporal, spectral, and spatial characteristics. To relate this work to existing theoretical models of IPS, the tri-factor model of IPS in MS is used (Costa et al. 2017). Our analysis gives support to this model, disambiguating IPS as three contributing factors: sensory, cognitive, and motor speed. Combining the previously discussed results with the tri-factor model of IPS, a novel description of the network-level brain dynamics underlying the SDMT is proposed in Figure 9.

Although the SDMT is highly sensitive in capturing slowed IPS in MS, it should be acknowledged that the SDMT is not a pure measure of IPS (Sandry et al. 2021). Aspects such as visual scanning or motor dysfunctions influence the assessment of IPS (Benedict et al. 2017). This is particularly important when research focuses specifically on the cognitive impairments in neurological diseases such as MS. In theory, one could extract the pure cognitive speed component by isolating the sensory

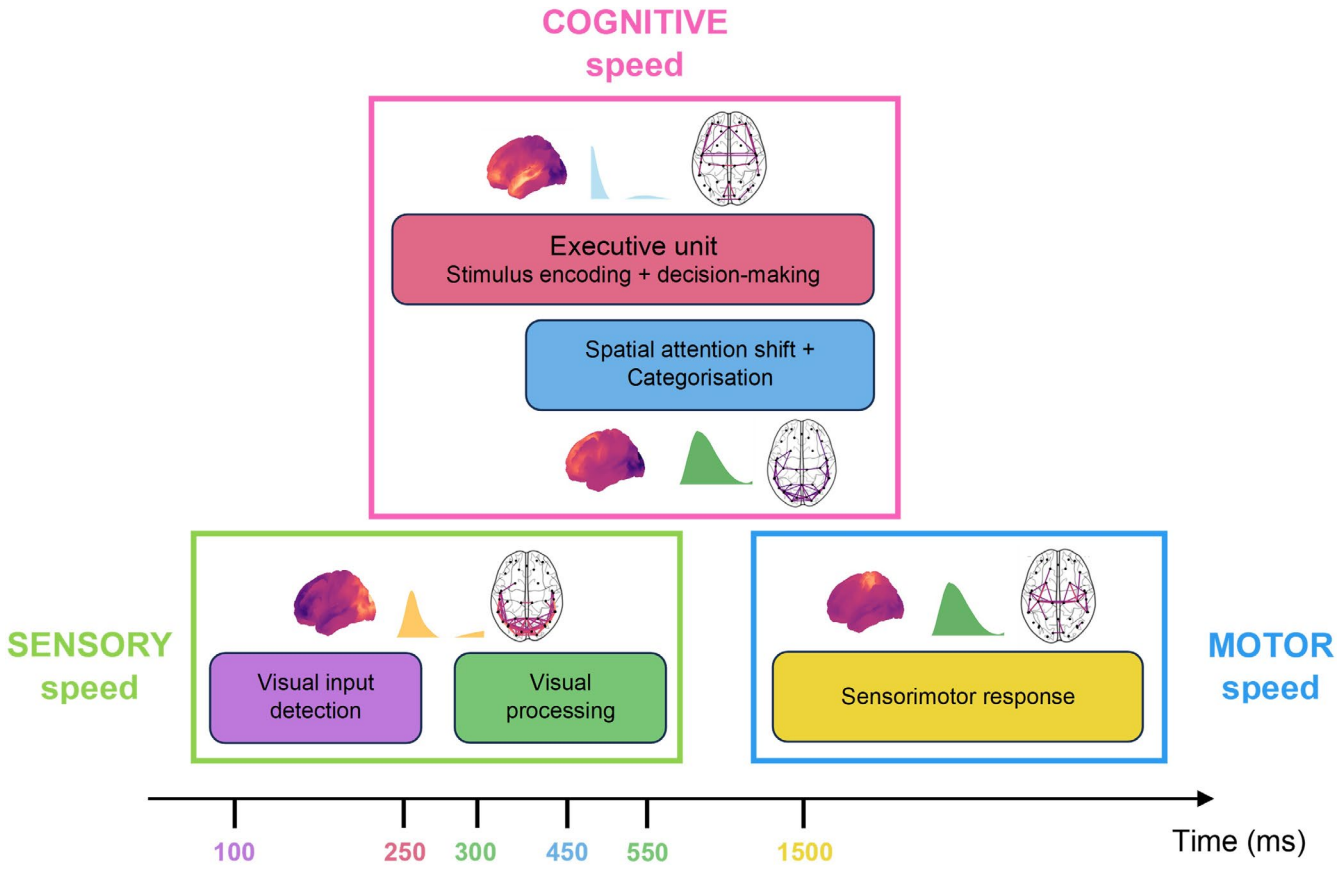

FIGURE 9 | Summary of the proposed pathway of the network-level brain dynamics unfolding during the computerised SDMT. The rectangles with filled colours and the numbers on the time axis are colour-coded to match the respective states sharing the same colours in Figures 4 and 5. Using the tri-factor model of IPS in MS (Costa et al. 2017), the pathway is divided into three parts: Sensory, cognitive, and motor speed.

and motor components contributing to IPS assessed by the SDMT. On the one hand, the sensory speed can be measured through the latency of VEPs (Baiano and Zeppieri 2024). On the other hand, the motor speed can be determined by means of transcranial magnetic stimulation (TMS) over the motor cortex (Spampinato et al. 2023). Future studies could explore this deeper by including additional experiments with the aim of isolating the targeted cognitive processing speed.

Previous work by Rossi et al. described the brain dynamics involved during a working memory (WM) task, the n-back (Rossi et al. 2023, 2024). Comparing the state descriptions between the n-back (WM task) and the SDMT (IPS task) reveals several brain states shared between both cognitive tasks, as well as task-unique states. Both tasks share a prefrontal theta, sensorimotor beta, and occipital alpha states. Specific to the n-back, Rossi et al. identified an M300 state important for memory recall and response selection. In our work, we identified a frontoparietal network, crucial for supporting attentional shifts between visual targets, unique to the SDMT. Not only can different tasks capture different task-specific cognitive processes, but they can also highlight similar network dysfunctions in PwMS. As such, prefrontal executive unit activation was revealed to be impaired in PwMS during both the n-back and SDMT.

A further consideration in interpreting our findings concerns the relationship between neural and cognitive slowing in MS and the extent to which our approach distinguishes them. Demyelination in MS directly impairs axonal conduction, leading to neuronal slowing that underpins global deficits in IPS. However, MEG analyses using the TDE-HMM, especially when performed during cognitive tasks like the SDMT, are optimised to detect dynamic changes in large-scale functional networks—reflecting cognitive slowing in domains such as attention, processing speed, and executive function. While these metrics are undoubtedly influenced by underlying neuronal pathology, their sensitivity lies primarily in revealing alterations to cognitive processes and adaptive network activity. Our results are therefore best interpreted as primarily reflecting cognitive slowing within a context of underlying neuronal deficits, with the most robust insights emerging when neural dynamics are interpreted in conjunction with behavioural performance measures.

5 | Limitations

In this work, we investigated MS-induced alterations in brain network activations within the extracted TDE-HMM states. Future studies should examine how these functional changes relate to structural MRI data. Given the key role of demyelination in IPS, incorporating MRI-derived structural measures could offer valuable insights into subject-specific disruptions of functional brain dynamics.

A limitation of the HMM is that the model assumes that only one state is active per time point, which may be too restrictive

to fully represent brain function. Dynamic Network Modes (DyNeMo), proposed by Gohil et al. (2022)., is a recently introduced technique that overcomes this limitation. Future studies could explore the DyNeMo approach to assess its potential to provide new insights regarding the network dynamics during execution of various cognitive tasks.

6 | Conclusion

This study provides a detailed description of the large-scale brain network dynamics underlying an IPS task. We applied the TDE-HMM method to task-MEG data, recorded while HCs and PwMS performed the SDMT. This revealed five task-relevant brain states with distinct temporal, spectral, and spatial characteristics. Analyses of peak features revealed reduced prefrontal activation in PwMS, with prefrontal, frontoparietal, and occipital network dynamics linked to task performance, including MEG-SDMT reaction times and clinical SDMT scores. In this way, our findings lend support to the tri-factor model of IPS in MS, which proposes that sensory, cognitive, and motor speed components collectively influence IPS assessments. The observed impairments, alongside the novel detailed network descriptions, can drive future research for treatments targeting the improvement of IPS performance.

Author Contributions

O.B. conducted the analysis and wrote the manuscript. J.V.S. was the main supervisor of the work and helped write and review the paper manuscript. F.A., C.R., D.V., and G.N. provided support regarding the analysis methods and provided comments during the manuscript writing. M.B.D. and M.D. provided comments on the work. All authors approved the submitted version.

Acknowledgments

The authors would like to thank all participants, both healthy controls and people with multiple sclerosis, for their time, enthusiasm, and dedication to this research. The MEG data collection was enabled by a grant from the Belgian Charcot Foundation and an unrestricted research grant by Genzyme-Sanofi awarded to G.N., who is a senior clinical research fellow of the Fonds Wetenschappelijk Onderzoek (FWO) Flanders (1805620N). O.B. is funded by FWO, under grant number 1109225N.

Funding

This work was supported by Fonds Wetenschappelijk Onderzoek, 1109225N, 1805620N.

Conflicts of Interest

The authors declare no conflicts of ineterst.

Data Availability Statement

The analyses were performed exclusively in Python using the osl-ephys (version 1.0.0) and osl-dynamics (version 1.4.5) packages. Both Python packages are publicly accessible on the OHBA Analysis Group GitHub: https://github.com/ohba-analysis. The contents of the performed analysis are based on the methodology reported by Quinn et al. (2018) and Rossi et al. (2024), together with example codes for the data preprocessing (https://github.com/OHBA-analysis/osl-ephys/tree/main/examples) and the TDE-HMM analysis (https://github.com/OHBA-analysis/osl-dynamics/tree/main/examples). Analysis scripts written in Python (Jupyter Notebooks) are available upon request from the corresponding author.

References

Alonso, S., and D. Vidaurre. 2023. "Toward Stability of Dynamic FC Estimates in Neuroimaging and Electrophysiology: Solutions and Limits." *Network Neuroscience* 7: 1389–1403.

Andersen, R. A., and H. Cui. 2009. "Intention, Action Planning, and Decision Making in Parietal-Frontal Circuits." *Neuron* 63: 568–583.

Antzoulatos, E. G., and E. K. Miller. 2016. "Synchronous Beta Rhythms of Frontoparietal Networks Support Only Behaviorally Relevant Representations." *eLife* 5: e17822.

Baiano, C., and M. Zeppieri. 2024. "Visual Evoked Potential." In *StatPearls*. StatPearls Publishing.

Baker, A. P., M. J. Brookes, I. A. Rezek, et al. 2014. "Fast Transient Networks in Spontaneous Human Brain Activity." *eLife* 3: e01867.

Barratt, E. L., P. K. Tewarie, M. A. Clarke, et al. 2017. "Abnormal Task Driven Neural Oscillations in Multiple Sclerosis: A Visuomotor MEG Study." *Human Brain Mapping* 38: 2441–2453.

Benedict, R. H., M. P. Amato, J. Boringa, et al. 2012. "Brief International Cognitive Assessment for MS (BICAMS): International Standards for Validation." *BMC Neurology* 12: 55.

Benedict, R. H., J. DeLuca, G. Phillips, et al. 2017. "Validity of the Symbol Digit Modalities Test as a Cognition Performance Outcome Measure for Multiple Sclerosis." *Multiple Sclerosis* 23: 721–733.

Bressler, S. L., and V. Menon. 2010. "Large-Scale Brain Networks in Cognition: Emerging Methods and Principles." *Trends in Cognitive Sciences* 14: 277–290.

Broche-Pérez, Y., L. F. Herrera Jiménez, and E. Omar-Martínez. 2016. "Bases neurales de la toma de decisiones." *Neurología* 31: 319–325.

Brookes, M. J., G. C. O'Neill, E. L. Hall, et al. 2014. "Measuring Temporal, Spectral and Spatial Changes in Electrophysiological Brain Network Connectivity." *NeuroImage* 91: 282–299.

Caffarra, S., K. Kanopka, J. Kruper, et al. 2024. "Development of the Alpha Rhythm Is Linked to Visual White Matter Pathways and Visual Detection Performance." *Journal of Neuroscience* 44: e0684232023.

Chiaravalloti, N. D., and J. DeLuca. 2008. "Cognitive Impairment in Multiple Sclerosis." *Lancet Neurology* 7: 1139–1151.

Corbetta, M. 1998. "Frontoparietal Cortical Networks for Directing Attention and the Eye to Visual Locations: Identical, Independent, or Overlapping Neural Systems?" *Proceedings of the National Academy of Sciences of the United States of America* 95: 831–838.

Corbetta, M., G. L. Shulman, F. M. Miezin, and S. E. Petersen. 1995. "Superior Parietal Cortex Activation During Spatial Attention Shifts and Visual Feature Conjunction." *Science* 270: 802–805.

Costa, S. L., H. M. Genova, J. DeLuca, and N. D. Chiaravalloti. 2017. "Information Processing Speed in Multiple Sclerosis: Past, Present, and Future." *Multiple Sclerosis* 23: 772–789.

Denney, D. R., S. G. Lynch, and B. A. Parmenter. 2008. "A 3-Year Longitudinal Study of Cognitive Impairment in Patients With Primary Progressive Multiple Sclerosis: Speed Matters." *Journal of the Neurological Sciences* 267: 129–136.

Dixon, M. L., R. Thiruchselvam, R. Todd, and K. Christoff. 2017. "Emotion and the Prefrontal Cortex: An Integrative Review." *Psychological Bulletin* 143: 1033–1081.

Dobson, R., and G. Giovannoni. 2019. "Multiple Sclerosis – A Review." *European Journal of Neurology* 26: 27–40.

Engelhardt, W., K. Friess, E. Hartung, M. Sold, and T. Dierks. 1992. "EEG and Auditory Evoked Potential P300 Compared With Psychometric

Tests in Assessing Vigilance After Benzodiazepine Sedation and Antagonism." *British Journal of Anaesthesia* 69: 75–80.

Forn, C., V. Belloch, J. C. Bustamante, et al. 2009. "A Symbol Digit Modalities Test Version Suitable for Functional MRI Studies." *Neuroscience Letters* 456: 11–14.

Foxe, J. J., and A. C. Snyder. 2011. "The Role of Alpha-Band Brain Oscillations as a Sensory Suppression Mechanism During Selective Attention." *Frontiers in Psychology* 2: 154.

Fuster, J. M. 2001. "The Prefrontal Cortex—An Update: Time Is of the Essence." *Neuron* 30: 319–333.

Genova, H. M., F. G. Hillary, G. Wylie, B. Rypma, and J. Deluca. 2009. "Examination of Processing Speed Deficits in Multiple Sclerosis Using Functional Magnetic Resonance Imaging." *Journal of the International Neuropsychological Society* 15: 383–393.

Gohil, C., R. Huang, E. Roberts, et al. 2024. "Osl-Dynamics, a Toolbox for Modeling Fast Dynamic Brain Activity." *eLife* 12: RP91949.

Gohil, C., O. Kohl, R. Huang, et al. 2024. "Dynamic Network Analysis of Electrophysiological Task Data." *Imaging Neuroscience* 2: 1–19.

Gohil, C., E. Roberts, R. Timms, et al. 2022. "Mixtures of Large-Scale Dynamic Functional Brain Network Modes." *NeuroImage* 263: 119595.

Grothe, M., M. Domin, K. Hoffeld, G. Nagels, and M. Lotze. 2020. "Functional Representation of the Symbol Digit Modalities Test in Relapsing Remitting Multiple Sclerosis." *Multiple Sclerosis and Related Disorders* 43: 102159.

Grothe, M., K. Jochem, S. Strauss, et al. 2022. "Performance in Information Processing Speed Is Associated With Parietal White Matter Tract Integrity in Multiple Sclerosis." *Frontiers in Neurology* 13: 982964.

Ichihara-Takeda, S., S. Yazawa, T. Murahara, et al. 2015. "Modulation of Alpha Activity in the Parieto-Occipital Area by Distractors During a Visuospatial Working Memory Task: A Magnetoencephalographic Study." *Journal of Cognitive Neuroscience* 27: 453–463.

Jensen, O., P. Goel, N. Kopell, M. Pohja, R. Hari, and B. Ermentrout. 2005. "On the Human Sensorimotor-Cortex Beta Rhythm: Sources and Modeling." *NeuroImage* 26: 347–355.

Julian, L. J. 2011. "Cognitive Functioning in Multiple Sclerosis." *Neurologic Clinics* 29: 507–525.

Kanishka, and S. K. Jha. 2023. "Compensatory Cognition in Neurological Diseases and Aging: A Review of Animal and Human Studies." *Aging Brain* 3: 100061.

Kiiski, H., L. Jollans, S. Ó. Donnchadha, et al. 2018. "Machine Learning EEG to Predict Cognitive Functioning and Processing Speed Over a 2-Year Period in Multiple Sclerosis Patients and Controls." *Brain Topography* 31: 346–363.

Kouvatsou, Z., E. Masoura, and V. Kimiskidis. 2022. "Working Memory Deficits in Multiple Sclerosis: An Overview of the Findings." *Frontiers in Psychology* 13: 866885.

Küchenhoff, S., C. Sorg, S. C. Schneider, et al. 2021. "Visual Processing Speed Is Linked to Functional Connectivity Between Right Frontoparietal and Visual Networks." *European Journal of Neuroscience* 53: 3362–3377.

Leavitt, V. M., G. Wylie, H. M. Genova, N. D. Chiaravalloti, and J. DeLuca. 2012. "Altered Effective Connectivity During Performance of an Information Processing Speed Task in Multiple Sclerosis." *Multiple Sclerosis (Houndmills)* 18: 409–417.

Liu, M., R. C. Amey, R. A. Backer, J. P. Simon, and C. E. Forbes. 2022. "Behavioral Studies Using Large-Scale Brain Networks – Methods and Validations." *Frontiers in Human Neuroscience* 16: 875201.

Meijer, K. A., Q. van Geest, A. J. C. Eijlers, J. J. G. Geurts, M. M. Schoonheim, and H. E. Hulst. 2018. "Is Impaired Information Processing Speed a Matter of Structural or Functional Damage in MS?" *NeuroImage: Clinical* 20: 844–850.

Middleton, R. M., O. R. Pearson, G. Ingram, et al. 2020. "A Rapid Electronic Cognitive Assessment Measure for Multiple Sclerosis: Validation of Cognitive Reaction, an Electronic Version of the Symbol Digit Modalities Test." *Journal of Medical Internet Research* 22: e18234.

Nichols, T., and S. Hayasaka. 2003. "Controlling the Familywise Error Rate in Functional Neuroimaging: A Comparative Review." *Statistical Methods in Medical Research* 12: 419–446.

Nuñez, A., and W. Buño. 2021. "The Theta Rhythm of the Hippocampus: From Neuronal and Circuit Mechanisms to Behavior." *Frontiers in Cellular Neuroscience* 15: 649262.

Pisarchik, A. N., V. A. Maksimenko, A. V. Andreev, et al. 2019. "Coherent Resonance in the Distributed Cortical Network During Sensory Information Processing." *Scientific Reports* 9: 18325.

Pokryszko-Dragan, A., M. Bilinska, E. Gruszka, E. Kusinska, and R. Podemski. 2015. "Assessment of Visual and Auditory Evoked Potentials in Multiple Sclerosis Patients With and Without Fatigue." *Neurological Sciences* 36: 235–242.

Polman, C. H., S. C. Reingold, B. Banwell, et al. 2011. "Diagnostic Criteria for Multiple Sclerosis: 2010 Revisions to the McDonald Criteria." *Annals of Neurology* 69: 292–302.

Quinn, A. J., D. Vidaurre, R. Abeysuriya, R. Becker, A. C. Nobre, and M. W. Woolrich. 2018. "Task-Evoked Dynamic Network Analysis Through Hidden Markov Modeling." *Frontiers in Neuroscience* 12: 00603.

Rocca, M. A., M. M. Schoonheim, P. Valsasina, J. J. G. Geurts, and M. Filippi. 2022. "Task- and Resting-State fMRI Studies in Multiple Sclerosis: From Regions to Systems and Time-Varying Analysis. Current Status and Future Perspective." *NeuroImage: Clinical* 35: 103076.

Rossi, C., D. Vidaurre, L. Costers, et al. 2023. "A Data-Driven Network Decomposition of the Temporal, Spatial, and Spectral Dynamics Underpinning Visual-Verbal Working Memory Processes." *Communications Biology* 6: 1–12.

Rossi, C., D. Vidaurre, L. Costers, et al. 2024. "Disrupted Working Memory Event-Related Network Dynamics in Multiple Sclerosis." *Communications Biology* 7: 1–16.

Sandry, J., D. V. Simonet, R. Brandstadter, et al. 2021. "The Symbol Digit Modalities Test (SDMT) Is Sensitive but Non-Specific in MS: Lexical Access Speed, Memory, and Information Processing Speed Independently Contribute to SDMT Performance." *Multiple Sclerosis and Related Disorders* 51: 102950.

Sarrias-Arrabal, E., S. Eichau, A. Galvao-Carmona, E. Domínguez, G. Izquierdo, and M. Vázquez-Marrufo. 2021. "Deficits in Early Sensory and Cognitive Processing Are Related to Phase and Nonphase EEG Activity in Multiple Sclerosis Patients." *Brain Sciences* 11: 629.

Schlaeger, R., M. D'Souza, C. Schindler, L. Grize, L. Kappos, and P. Fuhr. 2012. "Combined Evoked Potentials as Markers and Predictors of Disability in Early Multiple Sclerosis." *Clinical Neurophysiology* 123: 406–410.

Silva, P. H. R., C. T. Spedo, A. A. Barreira, and R. F. Leoni. 2018. "Symbol Digit Modalities Test Adaptation for Magnetic Resonance Imaging Environment: A Systematic Review and Meta-Analysis." *Multiple Sclerosis and Related Disorders* 20: 136–143.

Spampinato, D. A., J. Ibanez, L. Rocchi, and J. Rothwell. 2023. "Motor Potentials Evoked by Transcranial Magnetic Stimulation: Interpreting a Simple Measure of a Complex System." *Journal of Physiology* 601: 2827–2851.

Stadelmann, C., C. Wegner, and W. Brück. 2011. "Inflammation, Demyelination, and Degeneration—Recent Insights From MS

Pathology." *Biochimica et Biophysica Acta (BBA) - Molecular Basis of Disease* 1812: 275–282.

Steiger, J. H. 1980. "Tests for Comparing Elements of a Correlation Matrix." *Psychological Bulletin* 87: 245–251.

Strober, L., J. Englert, F. Munschauer, B. Weinstock-Guttman, S. Rao, and R. H. Benedict. 2009. "Sensitivity of Conventional Memory Tests in Multiple Sclerosis: Comparing the Rao Brief Repeatable Neuropsychological Battery and the Minimal Assessment of Cognitive Function in MS." *Multiple Sclerosis (Houndmills)* 15: 1077–1084.

Tamura, M., T. J. Spellman, A. M. Rosen, J. A. Gogos, and J. A. Gordon. 2017. "Hippocampal-Prefrontal Theta-Gamma Coupling During Performance of a Spatial Working Memory Task." *Nature Communications* 8: 2182.

van Es, M. W. J., C. Gohil, A. J. Quinn, and M. W. Woolrich. 2025. "osl-ephys: A Python Toolbox for the Analysis of Electrophysiology Data." *Frontiers in Neuroscience* 19: 1522675.

Van Schependom, J., M. B. D'hooghe, K. Cleynhens, et al. 2014. "The Symbol Digit Modalities Test as Sentinel Test for Cognitive Impairment in Multiple Sclerosis." *European Journal of Neurology* 21: 1219–1225.

Van Schependom, J., M. B. D'hooghe, K. Cleynhens, et al. 2015. "Reduced Information Processing Speed as Primum Movens for Cognitive Decline in MS." *Multiple Sclerosis (Houndmills)* 21: 83–91.

Van Schependom, J., D. Vidaurre, L. Costers, et al. 2019. "Altered Transient Brain Dynamics in Multiple Sclerosis: Treatment or Pathology?" *Human Brain Mapping* 40: 4789–4800.

Vidaurre, D., R. Abeysuriya, R. Becker, et al. 2018. "Discovering Dynamic Brain Networks From Big Data in Rest and Task." *NeuroImage* 180: 646–656.

Vidaurre, D., L. T. Hunt, A. J. Quinn, et al. 2018. "Spontaneous Cortical Activity Transiently Organises Into Frequency Specific Phase-Coupling Networks." *Nature Communications* 9: 2987.

Vidaurre, D., A. J. Quinn, A. P. Baker, D. Dupret, A. Tejero-Cantero, and M. W. Woolrich. 2016. "Spectrally Resolved Fast Transient Brain States in Electrophysiological Data." *NeuroImage* 126: 81–95.

Zhigalov, A., and O. Jensen. 2020. "Alpha Oscillations Do Not Implement Gain Control in Early Visual Cortex but Rather Gating in Parieto-Occipital Regions." *Human Brain Mapping* 41: 5176–5186.

Supporting Information

Additional supporting information can be found online in the Supporting Information section. **Table S1:** Bad channels and segments identified during MEG preprocessing. The values are reported as average proportions (%) across all subjects belonging to a certain group (mean ± std). Bad channel proportions are expressed against the total number of channels (magnetometer = 102, gradiometer = 204), and the proportions of rejected epochs containing a bad segment are expressed against the total 128 trials. Group comparisons (HCs vs. PwMS, and Scanner 1 vs. Scanner 2) were conducted using the Mann–Whitney *U*-test. $^*p < 0.05$. **Figure S1:** Accuracy distribution from the subjects' responses during the computerised SDMT. Pressing the wrong button or not pressing the button at all during the maximum allowed response window (6 s) is considered an incorrect response. Group differences between the different subgroups (HCs, PwMS, BZD+ and BZD−) were performed using the Mann–Whitney *U*-test. All *p*-values were FDR-corrected for multiple comparisons. Table S2 presents the results from a mixed two-way ANOVA to evaluate the significance of interactions between group- and paradigm condition effects on the response accuracy. Across all participants, the proportion of incorrect responses was slightly higher in Match trials (2.72% ± 2.70%) than in Non-match trials (2.45% ± 2.63%). However, this difference was not statistically significant (main effect of stimulus type: $F(1,108) = 0.90$, $p = 0.35$). Post hoc pairwise comparisons within each group confirmed that the difference in proportions of incorrect responses between Match and Non-match trials was not significant in HCs ($t(36) = -1.93$, $p = 0.06$) or PwMS ($t(72) = -0.27$, $p = 0.79$). In contrast, there was a significant main effect of disease, with PwMS making more errors overall than HCs ($F(1,108) = 6.16$, $p = 0.015$). Examination of the disease group × stimulus interaction showed that PwMS make significantly more errors than HCs only in Non-match trials ($t(107.26) = 3.04$, $p = 0.003$). **Table S2:** Incorrect response proportions during the computerised SDMT. Proportions are expressed in % (mean ± std). Group effects were modelled between-subjects (HCs vs. PwMS), paradigm condition effects were modelled within-subject (Match vs. Non-match trials), and their interaction was assessed using a mixed two-way ANOVA. All *p*-values (main effects and post hoc comparisons) were corrected for multiple comparisons through FDR correction. $^*p < 0.05$. Table S3 reports the mean RTs during SDMT execution, averaged across trials of the same stimulus type. Reaction times were generally longer for Non-match (1.82 ± 0.38 s) than for Match trials (1.67 ± 0.32 s) across all participants. This difference was highly significant, reflecting a strong main effect of stimulus type on mean RT ($F(1,108) = 167.01$, $p = 1e\text{-}23$), and remained significant within both HCs ($t(36) = 9.84$, $p = 9e\text{-}12$) and PwMS ($t(72) = 10.05$, $p = 2e\text{-}15$). Regarding the main effect of disease, PwMS responded significantly slower than HCs ($F(1,108) = 12.47$, $p = 6e\text{-}4$). This group difference was evident for both Match ($t(83.03) = 3.65$, $p = 5e\text{-}4$) and Non-match stimuli ($t(85.44) = 3.72$, $p = 4e\text{-}4$). Overall, these results indicate that both stimulus type and disease presence significantly influence reaction times during SDMT performance. **Table S3:** Mean reaction time (RT) during the computerised SDMT. Mean RTs are expressed in seconds (mean ± std). Only the correctly responded trials were included in computing the subject-level average RT. Group effects were modelled between-subjects (HCs vs. PwMS), paradigm condition effects were modelled within-subject (Match vs. Non-match trials), and their interaction was assessed using a mixed two-way ANOVA. All *p*-values (main effects and post hoc comparisons) were corrected for multiple comparisons through FDR correction. $^*< 0.05$. **Table S4:** Hyperparameters used for the data preparation and TDE-HMM inference process. The number of time-delay embeddings and number of principal components (PCs) for the PCA reduction step are used to prepare the parcelled MEG data before serving as input for model inference. The number of hidden states, number of random initialisations to provide initial values to the model parameters, sequence length expressed in samples, learning rate, batch size, and number of epochs are relevant for the TDE-HMM inference. We chose these hyperparameters according to the work and recommendations of Vidaurre, Hunt, et al. (2018). For the dataset used in this work, the loss function converged after about 30 epochs. **Figure S2:** Summary statistics for the extracted HMM states. The states' temporal characteristics are summarised by four metrics: Fractional Occupancy (FO), Mean Lifetime (MLT), Mean Interval (MI), and Switching Rate (SR). Violin plots show the distribution of the state's temporal properties across all subjects. **Table S5:** Quantified summary statistics for the extracted HMM states. The values are reported as averages of the states' properties across all subjects (mean ± std). Group comparisons (HCs vs. PwMS) were conducted using the permutation test with max *t*-statistic ($N = 1000$), and resulted in no significant group differences. **Table S6:** Regressor coding for the 2nd-level GLM. Experimental (stimulus type) and subject-specific (disease, medication, and gender) factors were modelled as categorical regressors in the 2nd-level GLM design. For group-level contrasts that rely on a single regressor (e.g., contrast C3: Disease effect, Figure S3), the contrast is always defined as (+1, −1), thereby contrasting the positive against the negative level. **Figure S3:** Group-level design matrix and contrast matrix. The design matrix (upper part) depicts the regressors as columns and the 220 observations (i.e., the subject-level event-related time courses) as rows. The colour coding reflects the actual regressor values (+1, −1, 0) of each observation, as specified in Table S6 (Supporting Information, Section 6). The contrast matrix (lower part) displays all contrasts together with the corresponding regressor weightings. Figure S4 reports the effect of several categorical regressors on the event-related state activation profiles. The stimulus type (Match or Non-match) does not modulate the states' activation profile (Figure S4a). Considering that subjects were asked to press a button during each trial and did not receive feedback on their

performance, this lack of effect between the two paradigm conditions seems reasonable. Looking at the disease effect plot, we observe several significant group differences between HCs and PwMS (Figure S4b). Specifically, certain time windows in states 1 and 5 show significantly reduced event-related state activation in PwMS compared to HCs, while state 3 exhibits significantly increased activation in PwMS throughout nearly the entire epoch window. These results were reported (see Figures 4 and 5) and further discussed in the main text. Regarding the effect of benzodiazepine uptake, we observed significantly increased activation in state 3 for the BZD+ PwMS group, only between 1200 and 1350 ms post-stimulus. Considering state 3's characteristic beta activity (Figure 3b), this supports the known effect of benzodiazepines in enhancing beta activity (Van Schependom et al. 2015; Engelhardt et al. 1992; van Lier et al. 2004). Rossi et al. reported a similar amplification of frontoparietal beta activity in BZD+ PwMS during the n-back task (Rossi et al. 2023). Lastly, a short-lived increase in state 3 activation was observed in females. **Figure S4:** Effect of group-level and experimental factors on the state activation profiles. In every subplot, each solid curve—associated to one state—represents the 2nd-level GLM contrast of parameter estimates (COPEs), expressed as the difference between two conditions, considered within (−500, 3000) ms around the stimulus onset. The evaluated contrasts are: (a) stimulus type effect (Non-match—Match), (b) disease effect (PwMS—HCs), (c) benzodiazepine effect within the MS cohort (BZD+ –BZD–), and (d) gender effect (female—male). The horizontal lines indicate time points of significant modulation of the state activation by the considered factor, determined using a permutation test ($N = 1000$) with the maximum t-statistic (corrected for multiple comparisons across states and time points) at a significance level of 5%. Figure S5 reports interaction effects between the categorical regressors stimulus type and disease, on the ER state activations. No significant modulation was found when evaluating the effect of stimulus type within either HCs or PwMS separately (Figures S5a and S5b). Regarding between-subject interaction effects, state 3 showed significantly higher activation in PwMS compared to HCs across several time windows, regardless of stimulus type (Figures S5c and S5d). State 5 showed a significant disease effect only for Non-match trials at early activation around 100 ms post-stimulus (Figure S5d). We also provide Figure S7, showing the same results plotted as group-averaged epochs for both conditions included in the contrasts, rather than directly plotting the COPEs (Supporting Information, Section 8). **Figure S5:** Effect of the stimulus type × disease interaction on the state activation profiles. In every subplot, each solid curve—associated to one state—represents the 2nd-level GLM contrast of parameter estimates (COPEs), reflecting the specified effect of interest, considered within (−500, 3000) ms around the stimulus onset. The evaluated contrasts are: (a) stimulus type effect only within HCs (Non-match—Match), (b) stimulus type effect only within PwMS (Non-match—Match), (c) disease effect only within Match trials (PwMS—HCs), (d) disease effect only within Non-match trials (PwMS—HCs). The horizontal lines indicate time points of significant modulation of the state activation by the considered factor, determined using a permutation test ($N = 1000$) with the maximum t-statistic (corrected for multiple comparisons across states and time points) at a significance level of 5%. **Figure S6:** Group-averaged epoch visualisation for the effect of benzodiazepines (C4) and gender (C5) on the states' activation profile. Each box is assigned to one of the states from the main analysis (6-state model) and displays two comparisons: benzodiazepine effect (BZD+ vs. BZD− PwMS) and gender effect (male vs. female), with solid lines representing the group-averaged epochs. Dotted vertical lines indicate the stimulus onset and mean reaction time, while pink shaded areas highlight time points where 2nd-level GLM contrasts reveal significant differences across groups (max t-stat permutation, $N = 1000$, $p < 0.05$). **Figure S7:** Group-averaged epoch visualisation of simple effects underlying the stimulus type × disease interaction (contrasts C6–C9) on the states' activation profiles. Each box is assigned to one of the states from the main analysis (6-state model) and displays four comparisons: Stimulus type effect within HCs (Non-match vs. Match), stimulus type effect within PwMS (Non-match vs. Match), disease effect in Match trials (PwMS vs. HCs), and disease effect in Non-match trials (PwMS vs. HCs), with solid lines representing the group-averaged epochs. Dotted vertical lines indicate the stimulus onset and mean reaction time, while pink shaded areas highlight time points where 2nd-level GLM contrasts reveal significant differences across groups (max t-stat permutation, $N = 1000$, $p < 0.05$). Figure S8 shows four spectral components obtained through data-driven spectral decomposition using non-negative matrix factorisation (NNMF). Spectral component 1 (blue) contains the delta (1–4 Hz) and theta (4–8 Hz) bands, forming the classical low-frequency bands. Spectral component 2 (yellow) represents the alpha band (8–13 Hz), and spectral component 3 (green) mainly captures the beta band (13–30 Hz). The fourth spectral component (purple) has been reported to capture high-frequency noise and is usually omitted during the states' description (Sarrias-Arrabal et al. 2021). **Figure S8:** Data-driven frequency bands ($N = 4$) obtained by spectral decomposition using non-negative matrix factorisation (NNMF). (a) All 4 extracted spectral components, (b) spectral component 1—associated with the low-frequency bands, (c) spectral component 2—represents the alpha band, (d) spectral component 3—captures the beta band. The last spectral component (SC4) filters high-frequency noise and is omitted in the states' frequency content description. **Figure S9:** Complete spectral description of state 1. Every column provides the spatial and spectral state description weighted by one of the three spectral components. The first row shows the considered spectral component, while the second row contains the associated spatial power map, where the PSD is standardised (z-score) across parcels. The last row displays the coherence networks thresholded using a GMM, shown on a circular plot and a brain mask. **Figure S10:** Complete spectral description of state 2. Every column provides the spatial and spectral state description weighted by one of the three spectral components. The first row shows the considered spectral component, while the second row contains the associated spatial power map, where the PSD is standardised (z-score) across parcels. The last row displays the coherence networks thresholded using a GMM, shown on a circular plot and a brain mask. **Figure S11:** Complete spectral description of state 3. Every column provides the spatial and spectral state description weighted by one of the three spectral components. The first row shows the considered spectral component, while the second row contains the associated spatial power map, where the PSD is standardised (z-score) across parcels. The last row displays the coherence networks thresholded using a GMM, shown on a circular plot and a brain mask. **Figure S12:** Complete spectral description of state 4. Every column provides the spatial and spectral state description weighted by one of the three spectral components. The first row shows the considered spectral component, while the second row contains the associated spatial power map, where the PSD is standardised (z-score) across parcels. The last row displays the coherence networks thresholded using a GMM, shown on a circular plot and a brain mask. **Figure S13:** Complete spectral description of state 5. Every column provides the spatial and spectral state description weighted by one of the three spectral components. The first row shows the considered spectral component, while the second row contains the associated spatial power map, where the PSD is standardised (z-score) across parcels. The last row displays the coherence networks thresholded using a GMM, shown on a circular plot and a brain mask. **Figure S14:** Complete spectral description of state 6. Every column provides the spatial and spectral state description weighted by one of the three spectral components. The first row shows the considered spectral component, while the second row contains the associated spatial power map, where the PSD is standardised (z-score) across parcels. The last row displays the coherence networks thresholded using a GMM, shown on a circular plot and a brain mask. **Table S7:** Mapping similar HMM states between two inferences. The subjects whose data was used for each inference were grouped by MEG scanner type (scanner 1 and scanner 2). Both models were trained using the same hyperparameters as in the main analysis (see Supporting Information, Section 4). **Figure S15:** State descriptions of the model inference in scanner 1 group. At the top, we plot the mean power spectral density (PSD) and mean coherence for all states as a function of frequency (broadband), obtained by averaging across subjects, and all regions (PSD) or pairs of regions (coherence). Shaded areas at each frequency bin correspond to the standard deviation across subjects. Then, each box displays the temporal and spatial description of a state. Regarding the temporal activation profile, we display two comparisons: disease group (HCs vs. PwMS) and paradigm

condition (correct vs. incorrect), with solid lines representing the group-averaged epochs. Pink shaded areas highlight time points where GLM contrasts reveal significant differences across groups or task conditions (max t-stat permutation, $N = 1000$, $p < 0.05$). The group-level average power is displayed on a spatial map, computed across the broadband frequency range (1–45) Hz, and standardised (z-score) across parcels. **Figure S16:** State descriptions of the model inference in scanner 2 group. At the top, we plot the mean power spectral density (PSD) and mean coherence for all states as a function of frequency (broadband), obtained by averaging across subjects, and all regions (PSD) or pairs of regions (coherence). Shaded areas at each frequency bin correspond to the standard deviation across subjects. Then, each box displays the temporal and spatial description of a state. Regarding the temporal activation profile, we display two comparisons: disease group (HCs vs. PwMS) and paradigm condition (correct vs. incorrect), with solid lines representing the group-averaged epochs. Pink shaded areas highlight time points where GLM contrasts reveal significant differences across groups or task conditions (max t-stat permutation, $N = 1000$, $p < 0.05$). The group-level average power is displayed on a spatial map, computed across the broadband frequency range (1–45) Hz, and standardised (z-score) across parcels. **Figure S17:** Correlation between peak latencies of late components in state 3 and state 5. Peak latencies were extracted at the maximum late activation in state 3 (850–1750 ms) and the minimum late deactivation in state 5 (1000–2000 ms), only for Match trials. The relationship is displayed as a scatter plot and regression line, and the correlation coefficient (r) was computed using Pearson's correlation.